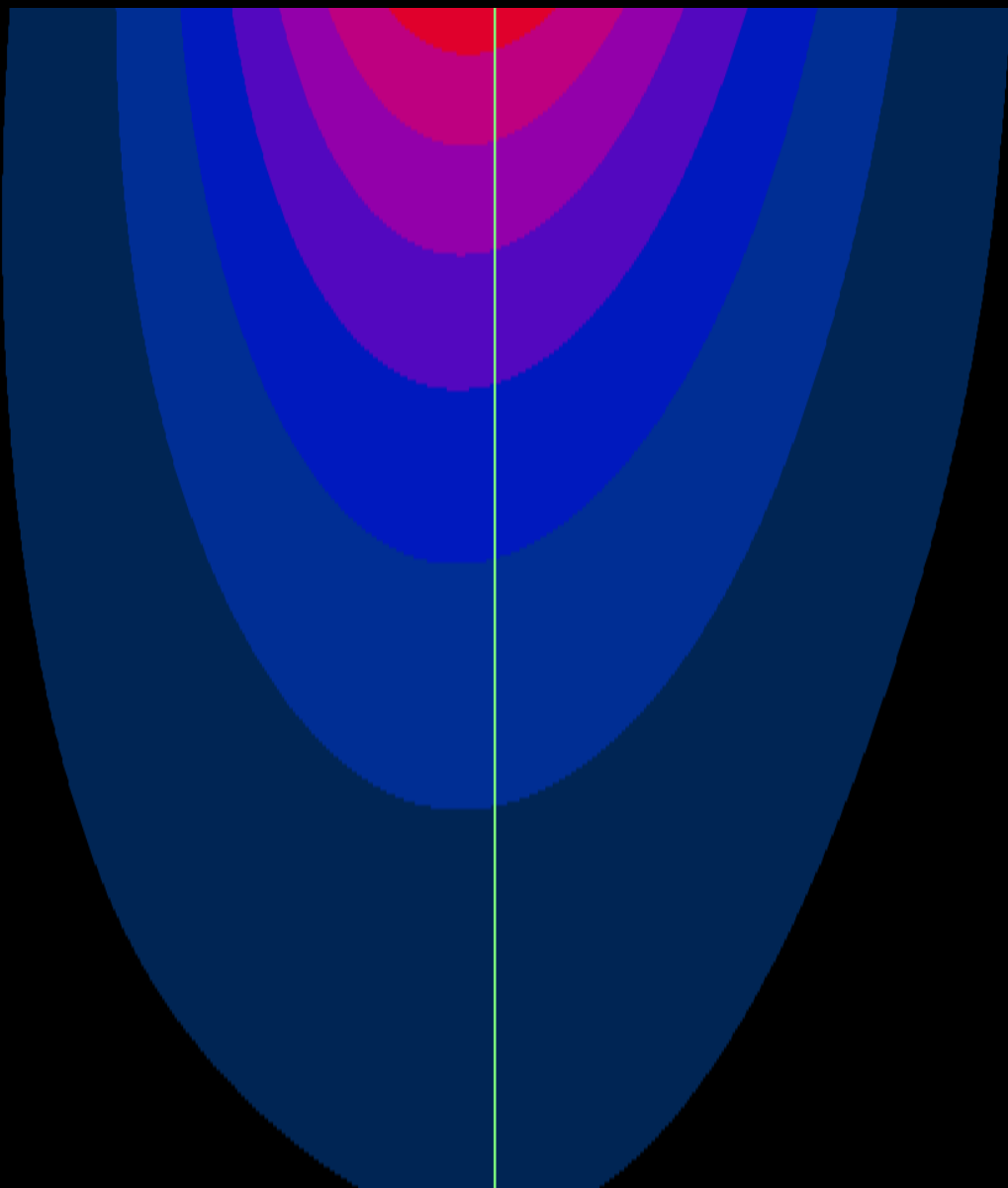


Optimizing a RF Coil for Prostate Imaging at 7 Tesla MRI

Alexa Viviana Obando Andrade

Master of Science Thesis



Optimizing a RF Coil for Prostate Imaging at 7 Tesla MRI

MASTER OF SCIENCE THESIS

For the degree of Master of Science in Biomedical Engineering at Delft
University of Technology

Alexa Viviana Obando Andrade

October 22, 2014

Faculty of Mechanical, Maritime and Materials Engineering (3mE) · Delft University of
Technology



University Medical Center
Utrecht



Copyright ©
All rights reserved.

DELFT UNIVERSITY OF TECHNOLOGY
DEPARTMENT OF

The undersigned hereby certify that they have read and recommend to the Faculty of
Mechanical, Maritime and Materials Engineering (3mE) for acceptance a thesis
entitled

OPTIMIZING A RF COIL FOR PROSTATE IMAGING AT 7 TESLA MRI

by

ALEXA VIVIANA OBANDO ANDRADE

in partial fulfillment of the requirements for the degree of

MASTER OF SCIENCE BIOMEDICAL ENGINEERING

Dated: October 22, 2014

Supervisor(s):

prof.Dr. Paddy French. Chairman

Dr.ir. Alexander Raaijmakers First Super

Dr.ir. Rob Remis Second Super

Reader(s):

Dr. Hans Zoetelief First Reader

Abstract

Ultra-high field prostate MR imaging ($\geq 7\text{T}$) becomes increasingly difficult due to insufficient radio frequency field excitation penetration [1]. RF coils used at ultra-high fields are adapted from lower field strengths but their performance is suboptimal. These coils are designed as near-field antennas; however, better signal penetration can be obtained using far-field concept, specifically in the case of prostate which is located deep in the body. In this project the optimization of an RF coil for prostate imaging at 7T Magnetic Resonance system is investigated. This RF coil was designed following far-field-based concept recently proposed by *Raaijmakers et al.* [2], who has demonstrated that higher transmit B_1 at depth can be obtained; thus increasing the transmit performance necessary to acquire good images. The RF coil consists of a fractionated dipole antenna mounted on an acrylic substrate, and it is used as part of a surface array. The optimization is evaluated in terms of safety (local SAR), transmit performance (B_1^+), and coupling measurements. A parameters study was performed to improve the performance of the RF coil. Numerical simulations were used to evaluate new designs obtained from the parameters study. From the simulated results, three designs were constructed for validation purposes. Two different measurements were performed to validate the simulations: B_1 measurements in the 7 Tesla MR scanner and coupling measurements with a network analyzer; these measurements were performed on a phantom with tissue electrical properties. Finally, an *in vivo* measurement using two identical sinusoidal-shaped snake antennas (s20) aligned on the pelvis was performed to image a healthy prostate. Both, simulations and measurements in the snake antennas demonstrated that despite the improvement gained in safety with lower levels of SAR, the radiation field penetration pattern is less homogeneous affecting the imaging process. Therefore, these antennas might show more efficiency imaging regions of interest where safety has to be ensured such as the heart, but for prostate imaging the fractionated dipole is preferable.

Table of Contents

Preface	xi
Acknowledgements	xiii
1 INTRODUCTION	1
1-1 Research Objective	2
2 Magnetic Resonance Imaging -MRI	3
2-1 MRI Principles	3
2-1-1 MRI Hardware Setup	4
2-1-2 Proton Spin	4
2-1-3 MRI Physics	5
2-1-4 MR Safety	7
2-2 Ultra-High Field MRI	8
2-2-1 Advantages of UH Field MR Systems	8
2-2-2 RF Challenges in UH Field MR Systems	9
2-2-3 RF Coil Design	9
3 METHODS AND MATERIALS	11
3-1 FDTD Simulations	11
3-1-1 Dipole Study Simulations	13
3-1-2 Fractionated Dipole with Meanders Study Simulations	13
3-1-3 Special Case: Sinusoidal Antennas	16
3-2 RF Coil Measurements	16
3-2-1 Construction of Phantom Setup For Measurements	16
3-2-2 FDTD Validation Simulations	18
3-2-3 B_1^+ Mapping Method	19
3-3 Data Validation	20
3-3-1 In Vivo MR Imaging	20

4	RESULTS	23
4-1	RF Antennas Simulation Results	23
4-1-1	Dipole Simulation Results	23
4-1-2	Fractionated Dipole Parameters Simulation Results	26
4-1-3	Special Case: Sinusoidal Antennas Simulation Results	33
4-2	RF Antenna Validation	35
4-2-1	Dipole Validation	35
4-2-2	Sinusoidal Antennas Validation	35
4-2-3	In Vivo Measurement	35
5	DISCUSSION AND CONCLUSIONS	39
5-1	Discussion	39
5-1-1	Dipole Discussion	39
5-1-2	Fractionated Dipole Parameters Study Discussion	40
5-1-3	Sinusoidal Antennas Discussion	41
5-1-4	Simulation Limitations	42
5-2	Conclusions	43
5-3	Recommendations	44
A	Sinusoidal Shaped Antennas	45
B	Construction of the phantom	49
C	Actual Flip Angle Imaging Method	51
D	Data from SEMCAD X Simulations	53
E	Mondrian Antenna	61
	Bibliography	63

List of Figures

2-1	Overview of the main components of an MRI scanner	4
2-2	Coordinated system [3]	5
2-3	Proton spin alignment when placed in a strong static magnetic field B_0 [3] . . .	5
2-4	Simulated MR images showing the effect of B_1^+ inhomogeneities as function of field strength [4]	8
2-5	Arrays from Erwin L. Hahn Institute for MRI, Essen, Germany. (a) 8-channel torso array. (b) 16-channel array [4]	10
3-1	RF coils simulated in SEMCAD X	12
3-2	Variation in the number of meanders, from zero to 16 meanders, conductor length constant (30cm)	14
3-3	Variation in form of meanders	15
3-4	Variation in the position of the meanders, conductor length constant (30cm) . .	15
3-5	Different sinusoidal shaped designs simulated	16
3-6	Circuit board of the dipole antenna matched using a perspex substrate of 10mm thickness (coronal view)	17
3-7	Printed circuit board of the matched snake antennas to be used for validation with the phantom (coronal view)	17
3-8	Validation setup in SEMCAD X, consisting of phantom, antenna, and shielding .	18
3-9	Simulated antennas for validation step	19
3-10	Setup used for validation	20
3-11	Setup for coupling measurement using an aquarium phantom and two identical snake antennas with 20mm thickness substrate (coronal view)	21
4-1	Simulated B_1^+ distributions in the transversal z-plane and sagittal y-plane directly below the element, linear color scale, normalized for 1 Watt delivered power. (a) dipole 5cm length, (b) dipole 25cm length, and (c) dipole 45cm length.	24

4-2	Simulated B_1^+ profiles from an ideal dipole antenna varying the length of the conductor from 5cm to 45 cm in 5cm steps. Normalized to 1 Watt delivered power.	24
4-3	Simulated local SAR distributions in the coronal x-plane and the transversal z-plane directly below the element, linear color scale, normalized for 1W of delivered power and averaged over 10g tissue. (a) dipole 5cm length, (b) dipole 25cm length, and (c) dipole 45cm length.	25
4-4	Calculated ratio local $SAR_{max}/(B_1^+)^2$ in function of the dipole length.	25
4-5	Simulated coupling measurements in the dipole antenna.	26
4-6	Simulated B_1^+ distributions in the coronal x-plane and transversal z-plane directly below the element, linear color scale, normalized for 1W delivered power in function of substrate thickness. (a) FDWM with substrate thickness 10mm, and (b) FDWM with substrate thickness 50mm	27
4-7	Simulated local SAR distributions in the coronal x-plane in function of substrate thickness, linear color scale, normalized for 1W of delivered power and averaged to 10g tissue (a) FDWM with substrate thickness 10mm, and (b) FDWM with substrate thickness 50mm	27
4-8	Simulated measurements for the fractionated dipole antenna	28
4-9	Simulated measurements varying the number of meanders	29
4-10	Simulated B_1^+ distributions in the coronal x-plane, linear color scale, normalized for 1W of delivered power. (a) fractionated dipole with meanders, and (b) form A	30
4-11	Simulated measurements varying the form of meanders	30
4-12	Simulated measurements varying the position of meanders where (P1) extremes of the conductor (P2) middle (P3) near the source	31
4-13	Simulated B_1^+ distributions of a dipole in the coronal x-plane and transversal plane y-plane varying the length of the conductor using perspex as substrate material, linear color scale, normalized for 1W of delivered power. (a) dipole 15cm length (b) dipole 30cm length and (b) dipole 45cm length	32
4-14	Simulated measurements varying the length of the conductor with perspex as substrate material	33
4-15	Simulated B_1^+ distributions of a dipole in the coronal x-plane and transversal plane y-plane varying the length of the conductor using perspex as substrate material, linear color scale, normalized for 1W of delivered power. (a) dipole 15cm length (b) dipole 30cm length and (b) dipole 45cm length	34
4-16	Simulated measurements of different sinusoidal shapes compared with the fractionated dipole (dark colors)	34
4-17	Validation of B_1^+ measurement of the dipole antenna	36
4-18	Simulated versus measured coupling in a dipole antenna of 30cm length and 10mm substrate thickness	37
4-19	Validation of B_1^+ measurement for two snake antennas s11 and s20	37
4-20	Simulated versus measured coupling in two snake antennas s11 and s20	38
4-21	Imaging results of array of two sinusoidal shaped antennas on a volunteer. Gradient Echo (GRE) transverse image of prostate and pelvis; TE/TR= 1.44/20 ms; resolution: $1 \times 1 \times 5 \text{ mm}^3$; NSA=2 (Number of Signal averages)	38
5-1	Voxelization step in SEMCAD X	42

A-4	Simulated sinusoidal antenna designs	48
B-1	Phantom used for B_1^+ measurements in the 7T MR system	49
B-2	Small phantom for permittivity measurements	50
C-1	MR Image showing a black ring	52
D-1	Variation in the form of the meanders first group of simulations	56
E-1	Mondrian Antenna	61

List of Tables

2-1	Larmor frequencies at common MRI field strengths	6
D-1	Simulated B_1^+ normalized to 1 Watt delivered power, simulated average SAR_{max} and calculated ratio average $SAR_{max}/(B_1^+)^2$ in function of the dipole length . .	53
D-2	Simulated coupling at different mutual distances in function of the dipole length	54
D-3	Simulated B_1^+ normalized to 1 Watt delivered power, simulated average SAR_{max} values normalized to 1W delivered power and calculated ratio average $SAR_{max}/(B_1^+)^2$ in function of the substrate thickness	54
D-4	Simulated coupling at different mutual distances in function of the substrate thickness	54
D-5	Simulated coupling in function of the substrate thickness	55
D-6	Simulated B_1^+ normalized to 1 Watt delivered power, simulated average SAR_{max} values normalized to 1W delivered power and calculated ratio average $SAR_{max}/(B_1^+)^2$ in function of the number of meanders	55
D-7	Simulated coupling in function of the number of meanders	55
D-8	Simulated B_1^+ normalized to 1 Watt delivered power, simulated average SAR_{max} and calculated ratio average $SAR_{max}/(B_1^+)^2$ in function of the form of meanders (substrate thickness 8mm)	56
D-9	Simulated B_1^+ normalized to 1 Watt delivered power, simulated average SAR_{max} and calculated ratio average $SAR_{max}/(B_1^+)^2$ in function of the form of meanders (substrate thickness 15mm)	56
D-10	Simulated B_1^+ normalized to 1 Watt delivered power, simulated average SAR_{max} and calculated ratio average $SAR_{max}/(B_1^+)^2$ in function of the position of meanders	57
D-11	Simulated B_1^+ normalized to 1 Watt delivered power, simulated average SAR_{max} and calculated ratio average $SAR_{max}/(B_1^+)^2$ in function of the form of meanders (substrate thickness 8mm)	58
D-12	Simulated B_1^+ normalized to 1 Watt delivered power, simulated average SAR_{max} and calculated ratio average $SAR_{max}/(B_1^+)^2$ in function of the form of meanders (substrate thickness 20mm)	59

E-1	Comparison of simulated results between Mondrian antenna, fractionated dipole and sinusoidal antenna	61
-----	--	----

Preface

The work for this thesis has been carried out at the site of the 7 Tesla MR scanner at the UMC in Utrecht. This exceptionally powerful scanner enables exploration of areas deeply located in the body such as the prostate through highly detailed images. This provides for instance the possibility of identifying prostate cancer.

For me working in a research facility such as 7 Tesla in the University Medical Center in Utrecht was an overwhelming experience that involved long days, simulations, constructing phantoms, matching antennas, and imaging but specially tons of new experiences and knowledge. I very much hope to keep on working in this particular field of study after I receive my master degree in Biomedical Engineering.

Acknowledgements

This thesis is the result of a long period of work from which I understood how challenging is going back to study. This project would not have been possible without the patience and support of many people. First of all, I would like to thank my supervisor dr.ir. Alexander Raaijmakers and dr.ir. C.A.T van den Berg for giving me the opportunity to work in this project and for their assistance and patience during this process. I cannot thank Alexander enough for all the explanations and time he spent helping me to understand the intricacies of Semcad X and 7T MR imaging. I would like to thank my colleagues at the UMC 7T lab (Ingmar, Michel, and Mark), also my office colleagues Astrid, Hanneke, and Deb for making me feel always welcome and for all the fun I had there. I am grateful to my supervisors in TU Delft dr.ir. Paddy French and dr.ir. Rob Remis for their helpful comments during the thesis. Also ir. Dinh Tran for his time and constant encouragement.

I would like to thank my family: my parents, my aunts, my brother and cousins, none of this would have been possible without the love and support of all of you, I feel blessed to have them motivating me when I thought I could not make it, Big thanks for my friends in the Netherlands and in Colombia (Diego J., Daniel C. and Esteban G.) for all your support.

Finally I thank COLFUTURO who financed my master in the Netherlands, this experience has been amazing for both my professional and my personal life and they made it possible.

Delft, University of Technology
October 22, 2014

Alexa Viviana Obando Andrade

“The MRI has a repertoire of noises that resemble, in no particular order: a game-show buzzer for a wrong answer, urgent knocking, a modem from 1992, a grizzly-bear growl, and a man with a raspy voice shouting what sounds like mother cooler!”

— *A.J. Jacobs, Drop Dead Healthy: One Man’s Humble Quest for Bodily Perfection*

Chapter 1

INTRODUCTION

The use of magnetic resonance imaging (MRI) has increased over the past decades, becoming an useful tool in modern healthcare. One of the main advantages of MRI, is it does not involve ionizing radiation in contrast with other imaging techniques such as computed tomography (CT), X-rays, and positron emission tomography (PET). MRI is based on a physical phenomenon called nuclear magnetic resonance (NMR), and does not cause detrimental effects on the patient's health.

MR imaging research has already managed to increase the image quality and speed in image acquisition. Nowadays, the standard field strengths for clinical practice go from 1.5 to 3 Tesla, and MRI research focus is shifting towards the use of higher main magnetic fields (B_0) to increase MRI advantages: better signal to noise ratio (SNR), spatial resolution, and sensitivity among others [5]. Besides the main magnetic field (B_0), MR systems need a B_1 field which represents the excitation field that the nuclei experience. In contrast with the B_0 , the B_1 is not static but is in the radio frequency (RF) range, thus is often referred to as RF field. It's intensity is just a fraction of the B_0 field, typically in the range of 10 or 20 μ T. Despite these advantages provided by the use of higher main magnetic field strengths, imaging at 7 Tesla has to solve radio frequency problems such as reduced penetration and inhomogeneity of the RF field and tissue overheating in the region of interest (ROI) [6]. RF problems are produced by the frequency of operation (Larmor frequency), which increases with the main magnetic field strength causing the wavelength of the RF field to become smaller compared to body dimensions. In the case of prostate, these problems become increasingly challenging due to the its deep location in the body, thus necessitating the use of higher RF power so the B_1^+ field is reaching the prostate [7]. Increasing the RF power can result in higher levels of energy deposition (specific absorption rate, SAR) posing safety concerns due to local overheating on the patient. These RF challenges related to radio frequency can be summarized as creation of a penetrating and homogeneous RF excitation field (B_1) inside the region of interest, while maintaining low levels of energy deposition [8].

There are different methods to solve these RF related problems such as RF multi-transmit techniques and coil array design [9]. This project focuses on the latter, working with an RF coil designed for 7 Tesla. However, the RF coil arrays used for research in the beginning

were commercial coil designs adapted from lower field strengths such as loop, stripline, and microstrip [4, 10]. These adapted designs were not efficient enough and the RF coil arrays had to be designed specifically for higher frequencies, 300MHz in the case of 7 Tesla MRI systems.

A larger part of the available studies have focused on designing coils for accessible body regions [11, 12] while only a few published works aimed at prostate, mainly using surface coil arrays [13, 14, 7, 15]. Deeply located targets are outside the near-field region at 300 MHz and therefore, prostate imaging at 7 Tesla requires designing RF coils on different principles.

This work is based on an RF coil designed as a far field antenna, which is part of a surface array used for prostate imaging. This design is called **fractionated dipole with meanders** (in short: fractionated dipole) and its performance was evaluated in order to establish an optimum design. Throughout this document the terms RF coil and RF antenna are used interchangeably both referring to the fractionated dipole. For the optimization process some characteristics of the fractionated dipole were varied to observe its impact on the performance and efficiency of the RF coil. The evaluation of the coil design is summarized as follows: firstly is evaluated by SEMCAD X simulations as a single element mainly through two parameters: the RF field penetration (B_1^+) and the levels of local SAR. Secondly, a coupling measurement is performed to observe the coil performance as part of an array to complete the evaluation. The variation of the coil characteristics generated new designs, some of them showing improvements in comparison with the original design. After the design characteristics study, two antennas were considered optimum. These so-called two "*snake antennas*" were constructed to validate the simulated results by means of (B_1^+), and coupling measurements on a phantom. Once validated by the phantom measurements, one of the *snake antennas* were used as a surface array for prostate imaging on a healthy volunteer.

1-1 Research Objective

This thesis focuses on the optimization of an RF coil used for prostate imaging at 7 Tesla MR system. The main goal is to find an optimized design after a parameters study in terms of RF magnetic field performance while complying safety regulations. The following research tasks must be completed in order to fulfill this project goal:

- Realize a parameter study to find the parameters with more influence in the efficiency and power deposition of the RF coil.
- Analyze the simulated data from the parameters study and find an optimum design.
- Construct the RF coils found optimum to validate the results obtained from the simulations.

Magnetic Resonance Imaging -MRI

This chapter includes an overview of the extensive field of magnetic resonance imaging (MRI). The principle of MRI is touched upon, followed by the system components necessary to create MR images. The next section is MR safety with a focus on RF induced temperature rise. And finally a short section about antenna systems was also included to explain why this RF coil is designed as a far field antenna.

2-1 MRI Principles

Magnetic resonance imaging is the most recent medical imaging technique. Since its introduction in medical clinics during the 80s, millions of scans are prescribed per year. MRI provides information about changes in soft tissue structure and alterations inside internal organs assisting in the diagnosis and treatment of a wide range of diseases [16]. Actually, MRI is becoming more and more popular in medical healthcare because it does not show detrimental effect on patient health, in comparison with CT scan which uses radiation to obtain the images. MRI hardware research has focused in increasing the static magnetic field strength, this is beneficial for different parameters such as spatial resolution, signal to noise ratio and spectral resolution [5]. The actual clinical standard is 3 Tesla MR system, but this project employed a stronger 7 Tesla scanner, which is mainly used for research. The main limitation of an ultra high field MR system is its safety, especially while imaging organs located deep inside the body such as the prostate [17].

Magnetic resonance imaging is based on a physical phenomenon called nuclear magnetic resonance (NMR). NMR is concerned with the spin property of protons in our body. The spin of a proton can be visualized as a ball rotating about its axis, and thus has an angular momentum and a magnetic momentum μ . The spinning protons can be excited with a radio frequency (RF) pulse into a higher energy state, during which the energy is stored. After the exciting RF field is turned off, energy is released. This energy can be measured and provides the MR data. When spatial encoding is applied, an image from a certain part of the body can be produced [18]. The following sections will focus on the details of MRI, starting with

hardware system, and the physics of MRI: precession, Larmor resonance frequency, and the MRI signal.

2-1-1 MRI Hardware Setup

As depicted in figure 2-1 the MRI scanner includes the following hardware components: (1) the main magnet; (2) the radio frequency (RF) coils; (3) the gradient coils; and (4) the electronics to create the images. The main magnet creates a static magnetic field (B_0). Field strengths in MR scanners vary from 0.5 Tesla to 3 Tesla for clinical use and it goes up to 9 Tesla used for research. This field is created by a cooled superconducting magnet immersed in liquid helium, which is in permanent operation. The homogeneity of the magnetic field produced must be assessed to avoid distorted images. The function of the three set of gradient coils is to vary temporarily the magnitude of B_0 to encode spatial information. These gradient coils allow the system to select a certain region for imaging. The RF transmit antenna excites the protons in the subject, and is commonly known as coil in the MR literature. The electromagnetic signal produced from the protons as they return to equilibrium can be received by either the same coil or by a separated one. The scanning console performs the image reconstruction [19].

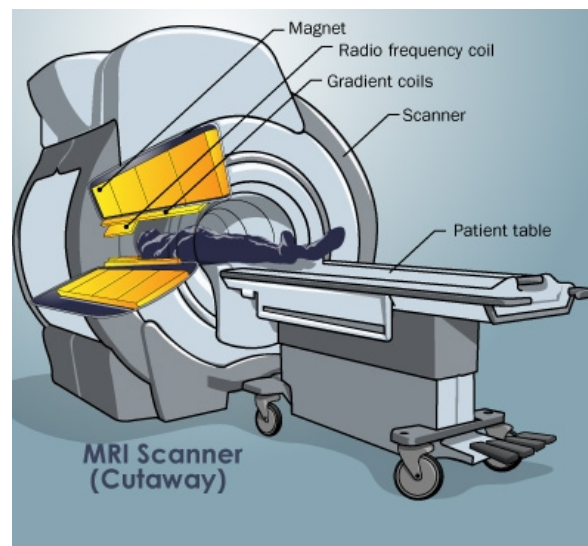


Figure 2-1: Overview of the main components of an MRI scanner

It is important to introduce a coordinate system, which will be a reference for radiation pattern images. For an MRI system the z-direction is horizontal and corresponds to the head to foot direction, which is the main magnetic field direction. The perpendicular plane to this direction is called the transverse plane or the x-y plane (figure 2-2).

2-1-2 Proton Spin

As mentioned earlier, protons with spin property have angular momentum and a magnetic moment μ . The proton rotates around its own internal axis with an angular momentum Φ , and as the proton is a charged particle this creates a small magnetic moment. The angular

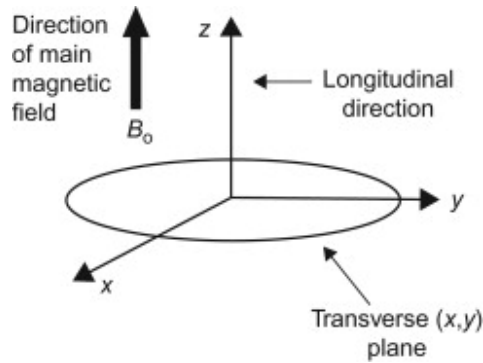


Figure 2-2: Coordinated system [3]

momentum is dependent on the strength of the magnetic field that is applied, and the magnetic moment is governed by the constant γ which is known as the gyromagnetic ratio described in equation 2-1.

$$\mu_{moment} = \gamma \Phi \quad (2-1)$$

Normally, spin protons are oriented randomly in space, thus the total magnetic moment will be zero. Instead, when the protons are placed in a strong magnetic field such as the MR scanner, some protons will tend to align in the direction of the magnetic field and some will tend to align in a direction opposite to the magnetic field. This parallel alignment results in a sum of single magnetization vectors called net magnetization (figure 2-3). This net magnetization becomes the source of the MR signal, and points parallel to the main static magnetic field [3].

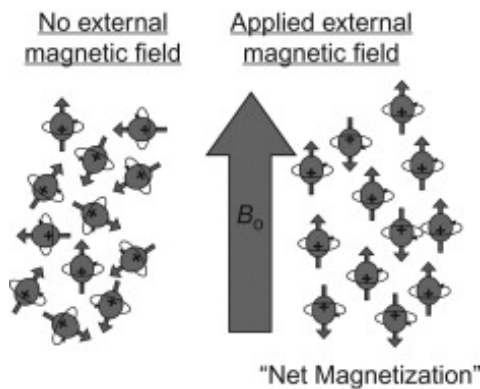


Figure 2-3: Proton spin alignment when placed in a strong static magnetic field B_0 [3]

2-1-3 MRI Physics

Larmor Resonance Frequency

The frequency of the rotation around the direction for the magnetic field is called precession or Larmor resonance frequency. This frequency is equal to the gyromagnetic ratio times the

main magnetic field strength (equation 2-2).

$$f_{Larmor} = \gamma B_0 (Hz) \quad (2-2)$$

This ratio is characteristic of each type of nuclei. For hydrogen protons, the gyromagnetic ratio is equal to 42.6 MHz/T. Hydrogen is used because it is present in very high density within the human body and thus provide a large enough signal to be detected. The resonant frequencies for hydrogen at different MR field strengths are given in the table 2-1

Table 2-1: Larmor frequencies at common MRI field strengths

Field strength B_0 (T)	Frequency (MHz)
1.5	64
3.0	128
7.0	298.2
9.4	400

The frequency of interest in this study is 298.2 MHz, the main frequency for the 7 Tesla scanner.

The Radiofrequency (RF) pulse

The RF pulse transmit RF energy which is absorbed by the proton spins. The transmitted magnetic field forces the net magnetization to rotate from the equilibrium direction. This amount of rotation is called flip angle and depends on the strength and duration of the RF pulse, therefore it is important to have equal flip angle excitation over the imaging region. After the excitation the magnetization vector return to its equilibrium, producing a magnetic field as a result. the magnetic field produced by applying the RF pulse is smaller compared to the main magnetic field B_0 generated by the superconducting magnet, and is called B_1 field. In general, the B_1 in frequency domain is defined as equation 2-3

$$B_1 = B_{1,x}i_x + B_{1,y}i_y + B_{1,z}i_z \quad (2-3)$$

The notation of the B_1 field is commonly split up in a portion that rotates with the Larmor frequency along with the precession of the protons (B_1^+) and a portion that rotates in the opposite direction (B_1^-). The B_1^+ field represents the excitation field that the nuclei experience, while the (B_1^-) field describes the behavior of the magnetic field in the receiving state. B_1^+ refers to the transmit component of the RF magnetic field vector, in contrast to the RF receive field B_1^- . A non uniform B_1^+ will create a distorted image because the flip angle distribution over the imaged volume will not be uniform. The two (B_1^+) and (B_1^-) can be written as function of the (B_1) field:

$$B_1^+ = \frac{B_{1,x} + iB_{1,y}}{2} \quad (2-4)$$

$$B_1^- = \frac{B_1, x - iB_1, y}{2} \quad (2-5)$$

The flip angle (α) is a function of pulse amplitude and excitation time length (τ). The time τ it takes for the magnetization vector to rotate an angle α is ideally instantaneous, though finite and bounded by the B_1^+ strength.

$$\alpha = \gamma B_1^+(x)\tau \quad (2-6)$$

High power RF pulses with peak power in the order of kilo watts are employed to reach the flip angle quickly.

Signal Detection

After the RF excitation, the protons will return from the higher energy state to equilibrium in the direction of the main magnetic field B_0 . This process is called relaxation and is described by the Bloch equations and consists of two relaxed phenomena: longitudinal relaxation (T_1) and transversal relaxation (T_2).

$$M_z(t) = M_0 \cos \alpha + (M_0 - M_0 \cos \alpha) \left[1 - \exp\left(-\frac{t}{T_1}\right) \right] \quad (2-7)$$

$$M_y(t) = M_0 \sin \alpha \left(\exp\left(-\frac{t}{T_2}\right) \right) \quad (2-8)$$

T_1 relaxation is called spin-lattice relaxation (M_z), and it influences the magnetization only in the z-direction (equation 2-7). It depends on the magnetic field strength and is related to the rate of regrowth of longitudinal magnetization. T_1 can be defined as the time necessary for the longitudinal magnetization to reach the 63% of its final value. T_2 or spin-spin relaxation relates to the decay of magnetization in the transverse plane after RF excitation. T_2 is defined as the time it takes for the transverse magnetization M_{xy} (equation 2-8) to decay to the 30% of the initial signal. Both time constants T_1 and T_2 are tissue specific and their values are in the order of milliseconds to seconds, in which T_2 is always shorter than T_1 . In low field MRI, the RF antenna is used for transmission and reception. However, with high field MRI two different coils are used [20].

2-1-4 MR Safety

The output peak power during excitation is in the order of kilo watts, this energy is dissipated in the tissues and can eventually lead to irreversible tissue damage [21]. The safety of the patient then must be insured while imaging at an MR system, to avoid possible tissue heating. Strict guidelines provided by the FDA are in place on the allowed power dissipated inside the body to prevent thermal injuries. The standards for RF safety use the Specific Absorption Rate (SAR), which is defined as a measure of the rate at which energy is absorbed by the body when exposed to a RF electromagnetic field (equation 2-9) and has units watt per kilogram (W/kg).

$$SAR = \frac{\sigma_E}{2\rho} |E|^2 = c \frac{dT}{dt} (W/kg) \quad (2-9)$$

where c is the specific heat capacity, σ_E is the electric conductivity, ρ the mass density of the tissue, \mathbf{E} the induced electric field vector and dT/dt the temperature increase in the tissue. Usually the global SAR over the whole body or body part is used. However, for smaller regions of interest such as the prostate a 10g or 1g local SAR average is preferred, since the global SAR will underestimate the maximum amount of local RF energy absorbed. In general, the SAR value depends heavily on the geometry of the part of the body that is exposed to the RF energy [22].

The center for devices and radiologic Health (CDRH) of the food and drug administration (FDA) has suggested limits on maximum SAR levels to be administered to patients during MRI examinations. The current suggested limits are 4 W/kg over any 15 min period for whole body SAR, 8 W/kg (12 in extremities) over 15 min period in any one gram of tissue, and 3 W/kg averaged over any 10 min for head SAR. The international electrotechnical commission (IEC) has published normal operating limits are 2 W/kg averaged over any 6 min period for whole body SAR, 3.2 W/kg averaged over any 6 min period for head SAR, and 10 W/kg in any 10 gram region of tissue in the head or torso (20 W/kg in any 10 gram region of tissue in extremities) averaged over any 6 min period [4].

2-2 Ultra-High Field MRI

Ultra-high field MRI refers to the main magnetic field strengths B_0 which 7 Tesla (300MHz) with a few systems operating at 9 Tesla (383MHz). The use of UH magnetic fields is expected to improve diagnosis, treatment monitoring and in the development of new therapies [7].

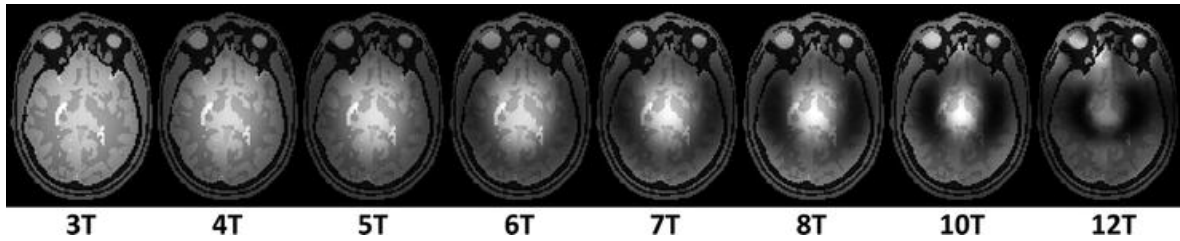


Figure 2-4: Simulated MR images showing the effect of B_1^+ inhomogeneities as function of field strength [4]

2-2-1 Advantages of UH Field MR Systems

There are several reasons for increasing the field strength in MR:

- **Enhanced sensitivity:** By using higher magnetic field (B_0) the spin polarization increases, increasing the signal to noise ratio (SNR) and resolution significantly [5].
- **Susceptibility:** it improves sensitivity making possible to realize vascular mapping.

- **Spectral resolution:** it allows to follow more complex changes in metabolites and amino-acids in vivo and non-invasively [23].
- **Parallel imaging:** it improves the excitation uniformity and coverage[12].

2-2-2 RF Challenges in UH Field MR Systems

MRI has to face also challenges, such as an increased severity of artefacts, higher motion sensitivity, increased sensitivity to physiological noise, and higher levels of RF heating [24],[25]:

- **RF inhomogeneity:** with increasing field strength, the Larmor wavelength for protons is reduced and, at 7T, approaches the dimensions of the human body and larger organs. This introduces significant and often unpredictable inhomogeneities in the MR images, which are dependent on tissue electromagnetic properties and considered to be a result of destructive B_1 interference [26].
- **Susceptibility effects:** it causes increased intravoxel signal loss and geometric distortion and, subsequently, reduced image quality in regions with large magnetic field inhomogeneities.
- **SAR effects:** higher magnetic field implies more power required to achieve the desired RF field penetration, resulting in increased tissue heating even in the absence of destructive interferences.

These challenges are more notorious for whole body imaging, and organs deep inside the body such as the prostate, specially RF penetration and the consequent inhomogeneous excitation of the body tissue. Some technical solutions to solve RF inhomogeneity involve multichannel transmit coils and the use of either static or dynamic RF shimming of the B_1^+ transmit field [24]. Another solution, is optimizing the coil array design to improve the RF field efficiency. This project is focused on optimizing an RF coil design.

2-2-3 RF Coil Design

The RF fields contain both an electric and a magnetic part, which interact with the body. However, the human body is composed of tissues that behave as a lossy dielectric material. The interactions between the RF wavelength and the tissue are ruled by the material they are crossing. The type of tissue determines the velocity of the wavelength. In general, the electromagnetic radiation cross vacuum at the same velocity of the light [27]. This velocity, c , is related to the electric permittivity of a vacuum (ϵ_0) and the magnetic permeability of a vacuum (μ_0) (equation 2-10):

$$c = \frac{1}{\sqrt{\epsilon_0 \mu_0}} \quad (2-10)$$

The velocity of the wavelength (λ) in a material depends on its frequency (equation 2-11). Thus, at higher frequencies, such as 300MHz in the case of 7T MR system, the wavelengths

becomes smaller making challenging imaging when the region of interest dimensions are larger, leading to a limited radiation field penetration, as is the case in whole body imaging or organs deeply located in the body such as the prostate. The permittivity in tissue has a wide range of values, therefore the wavelength in the body ranges from 12 to 17cm [28].

$$\lambda = \frac{c}{f}$$

$$\lambda_{tissue} \propto \frac{1}{f\sqrt{\mu_r\epsilon_r}} \quad (2-11)$$

The second factor to take into account in an RF coil design is the tissue conductivity (σ_E), because it affects the distribution of the B_1^+ , limiting its penetration. Besides, it has an impact on SAR and power deposition as it can be seen in the SAR equation (2-9). In resume, the main objective in high field coil design is to minimize the RF inhomogeneity and poor penetration while maintaining low SAR levels.

Surface Array Coils

At ultra-high magnetic fields, RF coils begin to behave less like energy conserving coils and more like energy radiating antennas [4, 29]. Prostate imaging is critical at 7T due to its location, more than one wavelength from the RF coil. In order to obtain good B_1^+ efficiency in the prostate, a different approach, designing this RF coil as a radiative antenna.

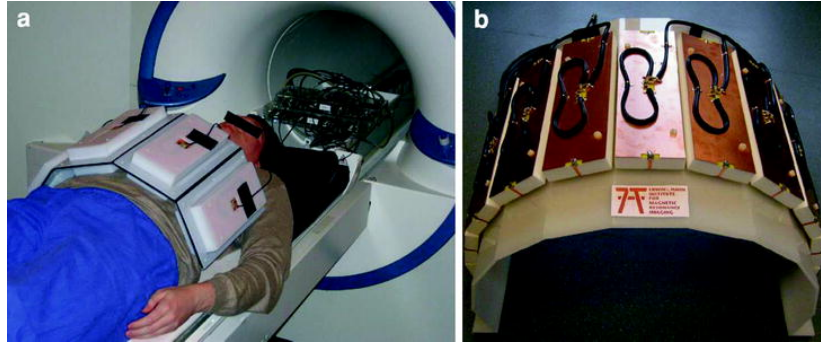


Figure 2-5: Arrays from Erwin L. Hahn Institute for MRI, Essen, Germany. (a) 8-channel torso array. (b) 16-channel array [4]

Some academic groups, primarily from the University of Minnesota and hospitals like UMC Utrecht and LUMC Leiden have been working on the adaptation of classical coils into multi-element transmit arrays (figure 2-5) for whole body, and prostate imaging at 7T MR systems.

METHODS AND MATERIALS

This research project focuses on the optimization of a RF coil called fractionated dipole with meanders (in short: FDWM) developed for prostate imaging in ultra-high field magnetic resonance imaging (UHF-MRI). This antenna was designed following antennas far field concept and it is operated in a surface array to overcome the reduced radio frequency field homogeneity and penetration present in a 7 Tesla Magnetic Resonance system. The main advantage obtained by this design is the combination of high RF penetration along with lower levels of energy deposition within the tissue compared with previous designs [10]. Despite its demonstrated benefits, further research is necessary to determine whether this antenna design is optimal. Optimization in the simulations is evaluated through three specific lines; performance, safety and interference [30]. The performance is evaluated from the magnetic field distribution, while the Average SAR is evaluated to ensure safe operating limits. The coils will be characterized by simulations, which will be validated with B_1^+ maps and coupling measurements, these measurements were performed to support simulation findings.

3-1 FDTD Simulations

RF simulations are widely used for ultra-high magnetic field strengths. At 300MHz the wavelength of the RF fields is shorter than the human body, making difficult to predict the interactions between RF waves and tissue analytically. Numerical simulations take into account these wavelength effects, which make them more accurate. In this project, all the coil designs were simulated using the Finite Difference Time Domain with SEMCAD X package (SPEAG, Schmid Partner Engineering, Zurich, Switzerland). This method solves Maxwell equations on a grid of voxels in an iterative way until it reaches a steady state [6].

Simulations were used to investigate the B_1^+ distribution, the SAR distribution, and the coupling between elements. This antenna is designed for prostate imaging mainly, therefore besides the B_1^+ profile, the B_1^+ values at 10 centimeters depth is also analyzed. Furthermore, the local SAR_{max} [IEEE/IEC 62704-1] is extracted for comparison of designs. The $B_{1at10cm}^+$ value and the local SAR_{max} level are used to calculate the local SAR over the excitation signal

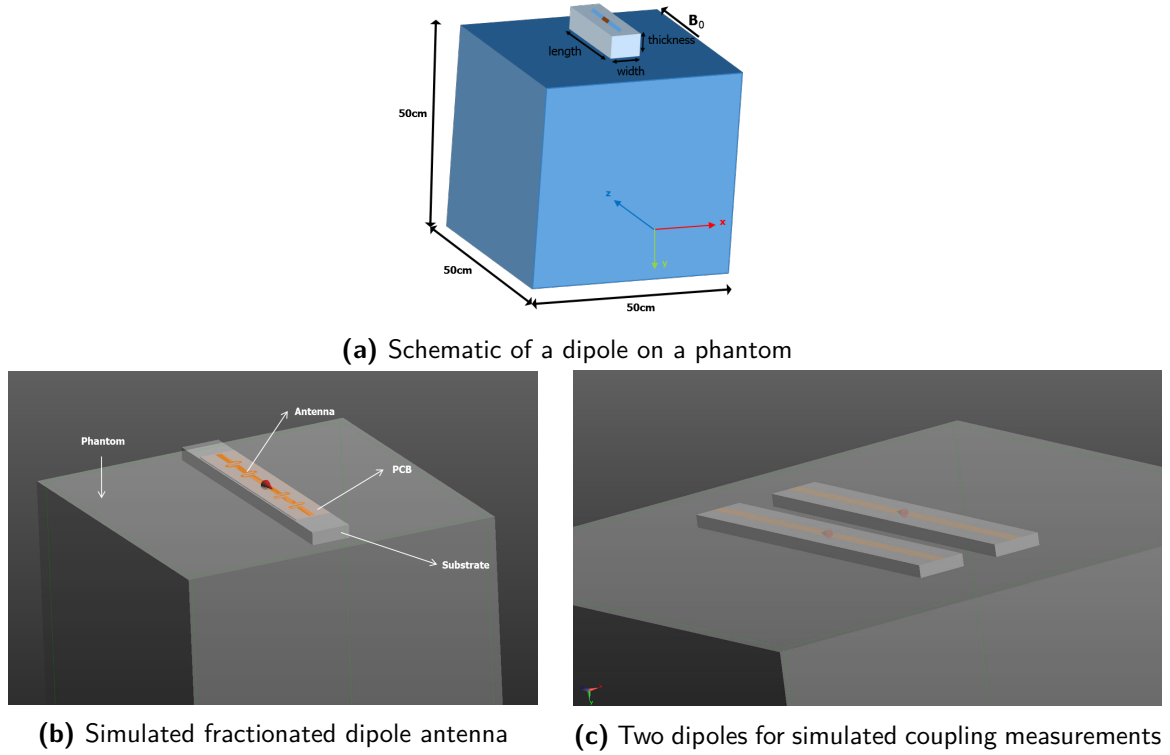


Figure 3-1: RF coils simulated in SEMCAD X

at depth local $SAR_{max}/(B_{1at10cm}^+)^2$. This ratio is calculated to evaluate the efficiency of a single element. Finally, coupling is measured between two identical coil elements to observe mutual interference and the ratio of transmitted and received power (S_{21}) is extracted in order to avoid destructive interference within the surface array.

The figure 3-1 shows a general setup which consists of a $50 \times 50 \times 50 \text{ cm}^3$ phantom with body equivalent dielectric properties ($\epsilon_r=34$; $\sigma = 0.4 \text{ S/m}$) where the coil element is located on top. Instead of using the body models provided by SEMCAD; a phantom was preferred due to its homogeneity, which makes B_1^+ and SAR distributions easier to compare without interference of tissue heterogeneities and shorter computing times. In the case of the coupling (figure 3-1c), two identical elements were simulated at different distances and S_{21} was evaluated. The grid resolution used in all cases was non uniform and mainly dependent on the geometry of the element simulated; always denser at the antenna location and surroundings than in the rest of the setup. The grid is evaluated by checking that the dimensions remain unchanged after the voxelization step. Also a connectivity check was performed after the voxelization step to ensure connections between conductors, the source and lumped elements if used. Results were extracted after performing a harmonic excitation at 298.2MHz with a simulation time of 10 periods. Computing time depends mainly on the grid size and minimum voxelization step.

The fractionated dipole with meanders is based on a basic dipole. For this reason and due to its basic geometry, the dipole was the first element simulated. The advantage of such simple design is that enables to find trends from design parameters variation and shows clearly their impact on the dipole efficiency. The second element simulated was the fractionated dipole.

A parameter study was performed to find an optimal design that combines B_1^+ efficiency with low power deposition in tissue. From this parameter study, sinusoidal-shaped antennas emerged and were simulated as a special case of the fractionated dipole.

3-1-1 Dipole Study Simulations

The dipole study is performed to investigate its benefits for magnetic resonance imaging and understand the contribution derived from the addition of the meanders to the dipole. This study investigates the impact of a change in two design parameters such as the length of the dipole, and the substrate thickness on the B_1^+ field, the SAR level, and the coupling. The length is varied from 2cm to 45cm in steps of 1cm; in each simulation the B_1^+ and SAR distributions were extracted, and the ratio was calculated from the values obtained previously. Note that both short/long length dimensions would be impractical for real use but a wide range can show how the B_1^+ radiation pattern change through length variation. In this case the substrate, consisting in an air gap between the dipole antenna and the phantom, was the second parameter investigated; this gap was modeled with air dielectric properties and varied from 10mm to 40mm in steps of 10mm. For coupling measurements besides the length and the air gap distance, the mutual distance between the two elements was studied, changing it from 4cm to 10cm. During each simulation, just one of the parameters was changed, while the others remained constant.

Dipole Antenna Design

The dipole antenna consists of two copper strips of 10mm width and variable length from 2cm to 45cm modelled as perfect electric conductors (PEC), with a space between conductors of 8mm; mounted on a substrate representing an air gap with a permittivity (ϵ) of 1, and a conductivity of $\sigma = 3 \times 10^{-15}$ S/m. The dipole is fed by a balanced signal between the copper strips. During the simulations the source impedance was not matched to the input impedance of the element. The grid for all the simulations was set in 3.83 Mcells with a minimum voxelization step of $1 \times 5 \times 1 \text{ mm}^3$.

3-1-2 Fractionated Dipole with Meanders Study Simulations

The fractionated dipole with meanders is an antenna designed using the far field concept for its use in prostate imaging in a 7T MR system; and it is part of an eight elements surface array. This element consists of a dipole with four meanders printed on a circuit board on an acrylic substrate. The meanders were added and successfully reduced SAR levels. During this project a design parameter study was performed to continue with the optimization process started by this addition. This parameter study consists of the variation of different design parameters like the length of the dipole, the thickness of the substrate, and some characteristics involving the meanders such as position, shape, and number. The impact of each parameter variation on the B_1^+ field, the SAR level is evaluated and an optimal value will be found by comparison. It is expected that the parameter study will provide a new design more efficient and depositing less energy than the original fractionated dipole.

Variation in substrate thickness

The first parameter to study is the thickness of substrate. In the case of the FDWM, (poly-methyl methacrylate -PMMA) known also as perspex is used as substrate material with a permittivity of 2.2 and a conductivity of 0.00022 S/m. This set of simulations uses the fractionated dipole with meanders maintaining its original length (30cm) and varies the thickness of the substrate. Two different electrical conductivity values of perspex were used, until $\sigma = 0.00022$ S/m was calculated for a frequency of 292.8MHz. The substrate width and length were kept constant and their variation is not included in this section. The substrate thickness was varied from 10, 15, 20, 30, 40, and 50mm. Simulated B_1^+ and SAR distributions, and coupling normalized to 1W delivered power were extracted using the general setup.

Variation in number of meanders

Since the meander addition to the dipole antenna proved to reduce SAR levels, it was considered important to investigate these structures further. Some characteristics such as number of meanders, the form, and the shape of the meanders were investigated. The number of meanders is varied starting from zero (plain dipole) 2, 4, 6, 8, and 16 meanders; keeping the total length of the conductor constant (30cm), and simulated using different substrate thicknesses of 15, 20 and 30mm. (Figure 3-2)

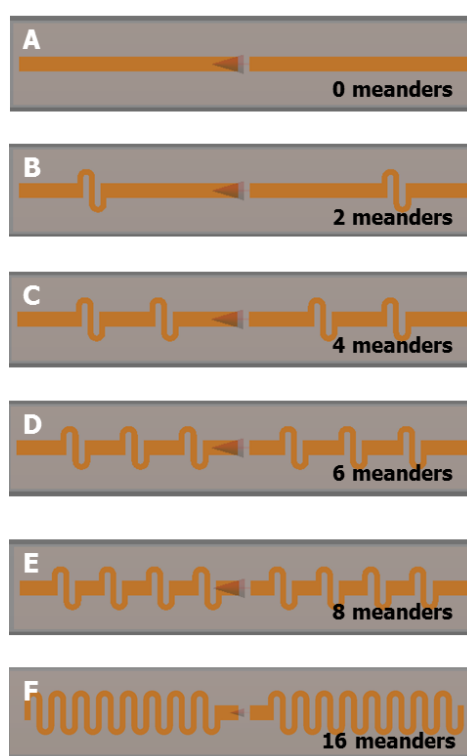


Figure 3-2: Variation in the number of meanders, from zero to 16 meanders, conductor length constant (30cm)

Variation in form of meanders

Some different shapes were tried just to observe whether the meander geometry affects the results. In this case, the total length of the conductor is constant (30cm) and a substrate thickness of 15mm is used. Firstly, the new forms were similar to the original meanders and the number did not vary. Combinations of large meanders and short meanders were also tried and the number of meanders also changed (figure 3-3). Finally, sinusoidal shapes were tried; they are explained extensively in the section 3.1.3 special case: sinusoidal shapes.

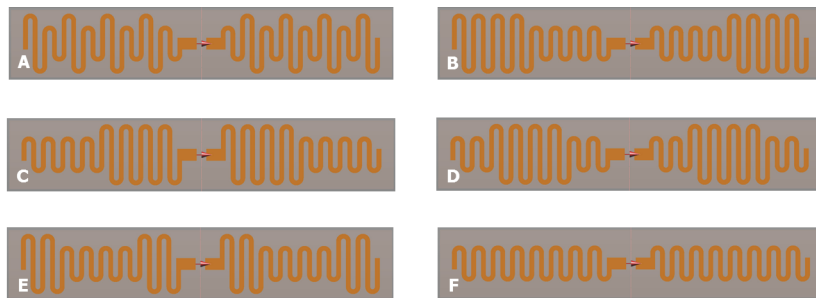


Figure 3-3: Variation in form of meanders

Variation in position of meanders

The position of the meanders was studied in a fractionated dipole with 2 meanders, one in each conductor. They were both positioned in the extremes of the conductor, in the middle and finally near the source. The total length of the conductor is constant (30cm) and a substrate thickness of 15mm is used. (Figure 3-4)

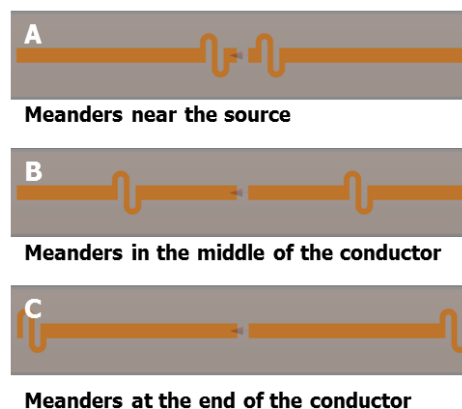


Figure 3-4: Variation in the position of the meanders, conductor length constant (30cm)

Variation in conductor length

In the dipole study the length is analyzed in an ideal case where the dipole is separated from the phantom by an air gap. In this case, a perspex substrate is used instead of an air

gap, and the length of the conductor is varied from 5cm to 45cm in steps of 1cm, keeping the space between conductors constant (8mm). It was preferred to use a dipole instead of the fractionated dipole to see the impact of the length in the measurements without the interference of the meanders using the same substrate material. Simulations with variable conductor length are using a plain dipole with a perspex substrate with 15mm thickness.

3-1-3 Special Case: Sinusoidal Antennas

The sinusoidal shapes are a special case derived while studying the form of the meanders. This study started varying the frequency or the amplitude of two basic sinusoidal shape antennas, followed by both variations being tried in one antenna. The total length of the antenna was kept constant in 30cm. Two substrate thicknesses were used; 8mm and 20mm. Around 23 different sinusoidal shapes were simulated using the general setup. The grid size varies for all cases therefore the connections and the dimensions of the antenna after the voxelization step had to be checked to guarantee correct measurements. Some of these sinusoidal shapes are shown in figure 3-5 [Appendix A]

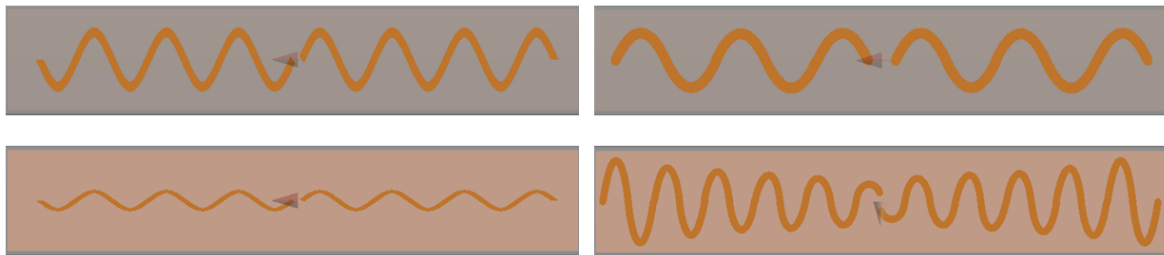


Figure 3-5: Different sinusoidal shaped designs simulated

3-2 RF Coil Measurements

After the extensive simulation studies, some of the antenna designs, along with a phantom were constructed to measure the B_1^+ field and the coupling to validate the results obtained from the simulations. SAR measurement was not performed, because temperature behavior is more difficult to measure in vivo. In this project, it was considered B_1^+ measurements would be enough to validate the results obtained from the simulations. This measurements were performed in the 7T MR system and the coupling measurements were performed in a network analyzer.

Different designs were constructed: from the dipole study a 30cm length dipole; and from the sinusoidal shape study, two sinusoidal-shape antennas (snake antennas) s11 and s20 respectively. Finally, an in vivo measurement with one of the snake antennas was performed in a healthy subject.

3-2-1 Construction of Phantom Setup For Measurements

As the antennas length is approximately 30cm length it was necessary to construct a phantom big enough to avoid reflections which can affect the measurement, under and around the

element. An acrylic aquarium of $22 \times 40 \times 25 \text{ cm}^3$ was filled with solution of agar in water (20g/L ; $5.7\text{mM } \text{CuSO}_4$) [Appendix B] with a permittivity of 80 and an electrical conductivity of 0.4 S/m approximately. The T_1 value of the phantom was determined independently at 205ms .

Antenna Designs for Measurements

The dipole antenna was designed and simulated in SEMCAD, exported to a circuit design program (Ultiboard - National Instruments), then grinded by a milling machine on a $60 \times 316 \times 2 \text{ mm}^3$ printed circuit board (PCB) (figure 3-6). In this case, the dipole is using a perspex substrate of $65 \times 320 \times 10 \text{ mm}^3$. The dipole was matched at 298.2MHz on the phantom using series capacitor values of 27 pF .

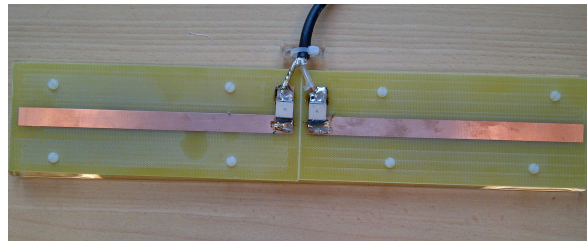
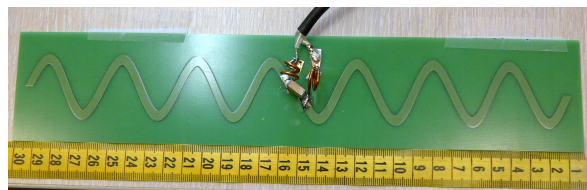
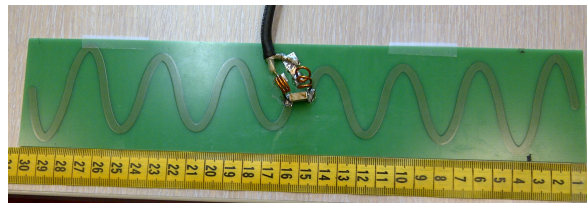


Figure 3-6: Circuit board of the dipole antenna matched using a perspex substrate of 10mm thickness (coronal view)

Both antennas were printed on a $60 \times 300 \times 1.5 \text{ mm}^3$ printed circuit board (PCB) with a green mask protecting the copper conductors. Both are using a perspex substrate of $65 \times 320 \times 20 \text{ mm}^3$. Finally they were matched at 298.2MHz on the phantom using capacitor values of 3.3pF for s11 and 5.6pF for s20 respectively. (Figure 3-7).



(a) Snake antenna S20



(b) Snake antenna S11

Figure 3-7: Printed circuit board of the matched snake antennas to be used for validation with the phantom (coronal view)

3-2-2 FDTD Validation Simulations

After the simulation of different designs, three antennas were chosen due to their performance to validate the results. For the validation step, besides the antennas a phantom was constructed. This new setup (figure 3-8) was simulated to be compared with the measurements obtained. It copies the geometry of a rectangular acrylic aquarium, full of gel with dielectric properties ($\epsilon_r = 80; \sigma = 0.4 \text{ S/m}$), and it uses smaller voxelization steps which makes the grid denser compared to the simulations performed with the first setup, leading to longer computing times.

The shielding induced by the scanner bore is also part of this setup in the form of a cylinder ($r = 58\text{cm}$) with perfect electric conductor (PEC) properties. The B_1^+ maps were extracted from the transversal slice (y-plane) and were normalized to 1W delivered power. The comparison between the data obtained from the simulations and the measurement was performed in Matlab (The Mathworks, Inc., Natick, MA, USA).

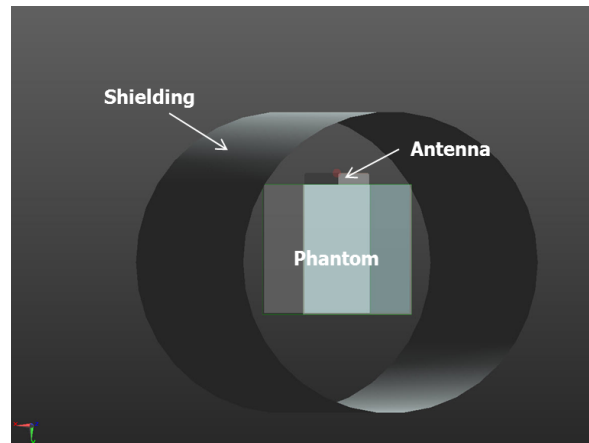


Figure 3-8: Validation setup in SEMCAD X, consisting of phantom, antenna, and shielding

Antenna Designs for Validation Simulations

A plain dipole of 30cm length with perspex substrate was chosen for construction according to the results given by the variation in the dipole length. It consists of a dipole on a printed circuit board (PCB) mounted on a substrate of 10mm thickness. The dipole consists of two copper bands of $10 \times 150 \text{ mm}^2$ modeled as 2D structures with perfect electric conductor (PEC) properties. The feeding source is located in the middle of the two conductors. The simulation was performed using the validation setup and a grid of 19.8Mcells. (Figure 3-9a)

Two of the sinusoidal shape antennas were constructed; s11 and s20 (figure 3-9b). These antennas use a substrate thickness of 20mm, and the antennas are mounted in a printed circuit board with the same specifications used in the simulated dipole design. The simulation was performed using a grid of approximately 27Mcells with minimum voxelization steps of $0.3 \times 1 \times 0.2 \text{ mm}^3$.

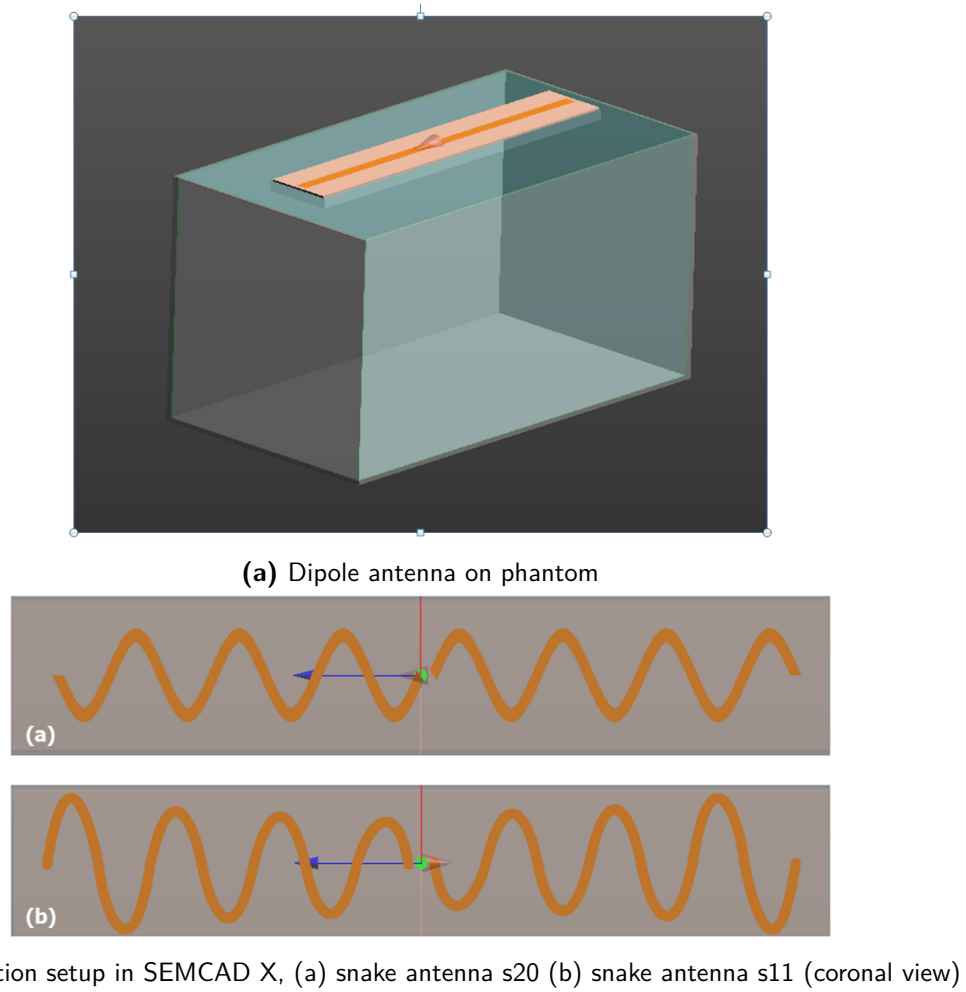


Figure 3-9: Simulated antennas for validation step

3-2-3 B_1^+ Mapping Method

The B_1^+ maps were acquired in the transverse plane of the aquarium phantom. The method used for B_1^+ mapping was actual flip-angle Imaging (AFI) [31]. This method gets fast image based measurements of the B_1 field, and consists in two gradient echo (GRE) acquired with identical RF pulses but two delay times of different duration TR_1 and TR_2 . AFI method makes some assumptions which have to be met to acquire a valid B_1^+ map using its approximation. The first assumption is that both delay times TR_1 and TR_2 are shorter than T_1 ; thus T_1 was measured in the aquarium phantom and has a value of approximately 205ms. The TR_1 and TR_2 used for B_1^+ mapping with AFI method were chosen as 10ms and 40ms, respectively with a flip angle of 65. [Appendix C].

3-3 Data Validation

The B_1^+ maps and the coupling measurements were performed to validate simulated data. The magnetic field measurements were performed in a Philips 7T Achieva MR scanner (Philips Healthcare, Cleveland, OH), where an aquarium phantom with an antenna on top was placed (figure 3-10). The B_1^+ distributions were acquired in the central transverse plane of the phantom. Each one of the antennas constructed; a dipole antenna with a perspex substrate (10mm) and two snake antennas (s11 and s20) with a perspex substrate (20mm) were investigated. Images from the 7T MRI were used to obtain the B_1^+ distributions, using gradient echo (GRE) technique; a sequence with increasing flip angles for imaging. The image resolution was $3.13 \times 3.13 \times 10 \text{ mm}^3$ approximately, and echo time/pulse repetition time (TE/TR) was 2.2/10 ms.

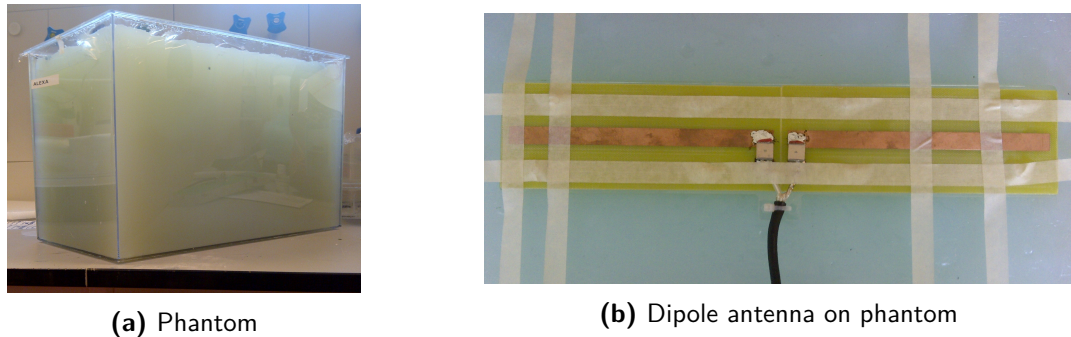


Figure 3-10: Setup used for validation

The comparison between the simulations and the measurements was performed in Matlab (The Mathworks, Inc., Natick, MA, USA). The simulation was exported from SEMCAD as a Matlab file of a transversal slide from the centre of the antenna, normalized to 1W delivered power. The distribution has a variable voxel size due to the heterogeneous grid used which is denser around the antenna; a function is needed to obtain a homogeneous distribution. This new homogeneous map is multiplied by the power obtained from the amplifier, this value was measured separately and was found to be 496 kW. This simulated B_1^+ distribution has a voxel size of 2mm and coincides with the size of the aquarium phantom, thus is now ready to be compared with the measurement. The files containing B_1^+ maps obtained from the 7T MRI measurements are rec-par, and processed in Matlab.

In addition, coupling was measured in all the three antennas constructed; with a vector network analyzer (Rhode & Schwarz ZVL frequency Range 9KHz - 3GHz) using two identical matched antennas, placed on the aquarium phantom (figure 3-11). Measurements were taken varying heart-to-heart distance from 7 to 10cm in steps of 1cm. The simulated coupling values were obtained using the simulated validation setup and compared with the measured values from the network analyzer.

3-3-1 In Vivo MR Imaging

The two sinusoidal shape antennas (s11 and s20) which gave the best results in terms of ratio and coupling were constructed to measure B_1^+ profiles and coupling with a phantom. After

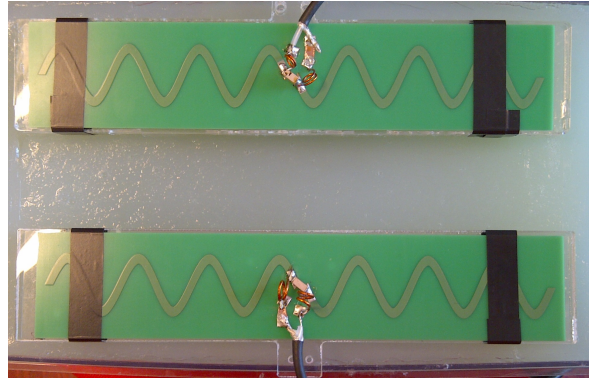


Figure 3-11: Setup for coupling measurement using an aquarium phantom and two identical snake antennas with 20mm thickness substrate (coronal view)

validating phantom simulations with B_1^+ and coupling measurements, antenna s20 showed more homogeneous radiation pattern and higher B_1^+ value at 10cm depth compared to s11. The snake antenna s20 is the chosen design to perform a volunteer imaging. Two identical elements (s20) were placed loosely on top of a healthy volunteer for prostate imaging. These antennas were matched using the phantom and their configuration was not changed to take this image. A gradient echo (T1W) image of prostate and pelvis in the transversal plane was recorded at a $1 \times 1 \times 5 \text{ mm}^3$ resolution with TE/TR= 1.44/20 ms and NSA=2 (number of signal averages).

Chapter 4

RESULTS

This chapter presents simulated results and measurements from different studies: one of a dipole antenna, fractionated dipole antenna parameters study and sinusoidal shaped antennas study. The coil elements with a better performance in terms of RF field radiation penetration and power deposition when compared with the fractionated dipole were constructed to validate the results obtained from FDTD simulations. B_1^+ and coupling measurements were chosen to validate data obtained from simulations, both measured on a phantom setup. Finally, one of these new coil elements was used for an in vivo prostate imaging.

4-1 RF Antennas Simulation Results

4-1-1 Dipole Simulation Results

For dipoles of 5cm, 25cm, and 45cm length, simulated B_1^+ distributions normalized to 1W delivered power are presented in figure 4-1. It shows the z-plane and the y-plane in the phantom at depth directly below the dipole antenna. The set of transversal images shows how the B_1^+ distribution is enlarged in z-plane along with the increment in the dipole length. The transversal images show the penetration is larger in the 25cm length dipole (centre-bottom) compared with 5cm and 45cm length respectively. Both planes depict the variation of the dipole length affects the B_1^+ distribution shape.

Figure 4-2a shows the B_1^+ profile, from 5cm length to 45cm length in 5cm steps versus depth of the phantom. The profile drops exponentially as it goes deep into the phantom; one can also infer that as the length increases the B_1^+ peak value decreases. For prostate imaging, 10cm depth is considered the position of the prostate within the body. Figure 4-2b shows the B_1^+ values at 10cm depth versus the dipole lengths; it can clearly be observed that the range from 15cm length to 25 cm length present the highest the B_1^+ values at 10cm depth. Optimization in case of the fractionated dipole with meanders requires maximizing B_1^+ value at 10cm depth while achieving lower values of SAR (specific absorption rate).

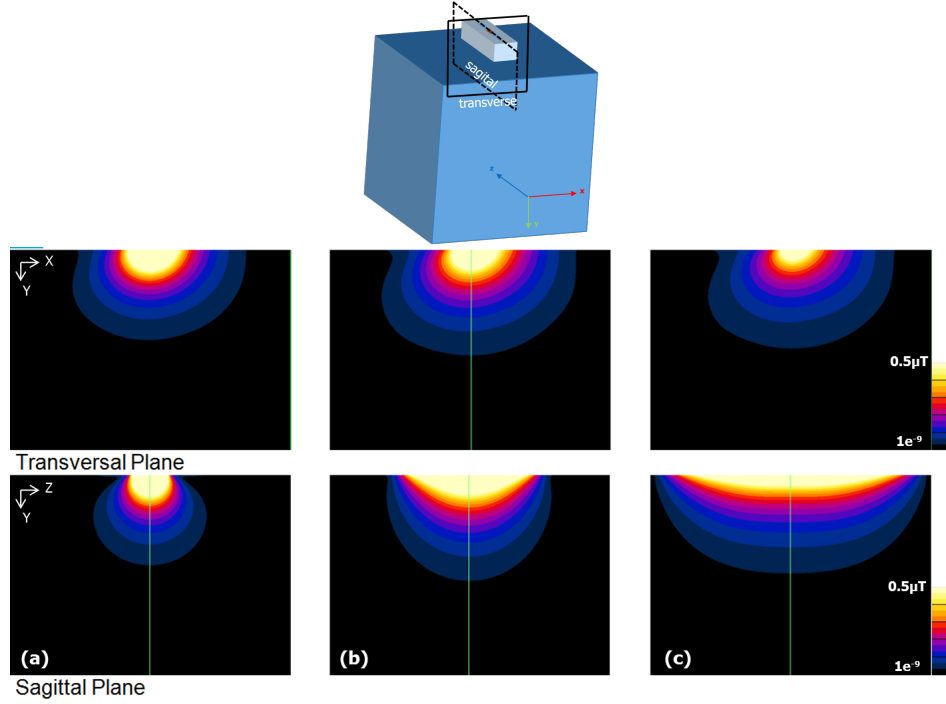


Figure 4-1: Simulated B_1^+ distributions in the transversal z-plane and sagittal y-plane directly below the element, linear color scale, normalized for 1 Watt delivered power. (a) dipole 5cm length, (b) dipole 25cm length, and (c) dipole 45cm length.

Figure 4-3 presents the simulated local SAR (specific absorption rate) (IEEE/IEC 62704-1) averaged over 10g and normalized to 1W delivered power in 5cm, 25cm and 45cm length dipoles. The local SAR was preferred instead of global SAR, because local SAR is a limiting factor for high field imaging (Metzger 2010, Ipek 2012). Both coronal and transversal planes show the local SAR decreasing as the length increases. The local SAR_{max} values for all the dipole lengths, presents downward trend with the peak at 5cm length dipole and the lowest value at 45cm length dipole.

The ratio $local\ SAR_{max}/(B_{1at10cm}^+)^2$ yields a balance between B_1^+ and local SAR_{max} values; a low value translates to efficiency in the performance of the antenna. For this reason, the ratio is one of the key values to determine the optimum dipole length range along with coupling. Figure 4-4 depicts the calculated ratio from 5cm length to 45cm, where the lower values



(a) B_1^+ profiles versus depth of the phantom **(b)** B_1^+ values at 10cm depth versus dipole length

Figure 4-2: Simulated B_1^+ profiles from an ideal dipole antenna varying the length of the conductor from 5cm to 45 cm in 5cm steps. Normalized to 1 Watt delivered power.

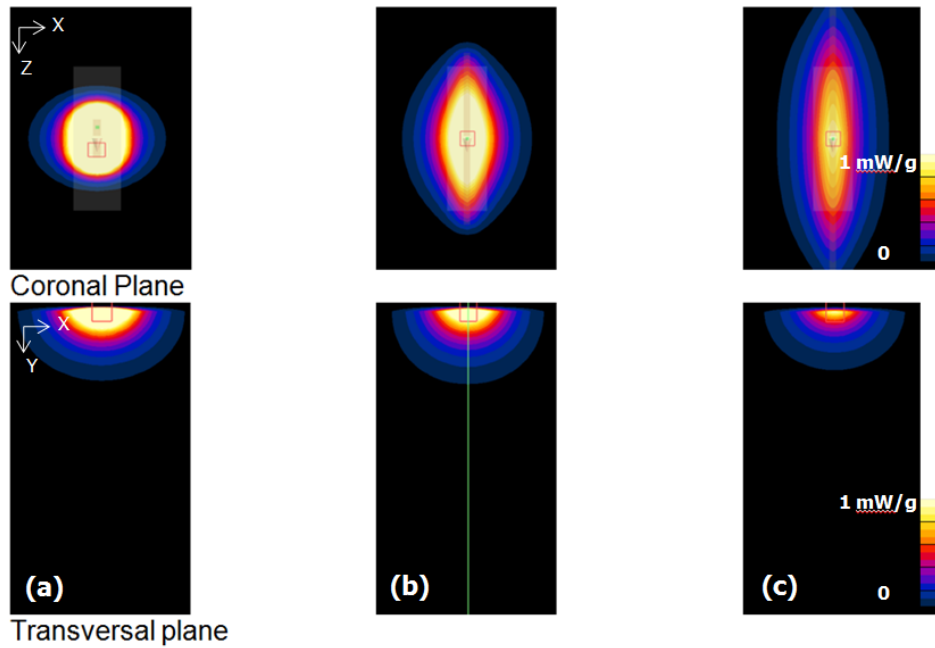


Figure 4-3: Simulated local SAR distributions in the coronal x-plane and the transversal z-plane directly below the element, linear color scale, normalized for 1W of delivered power and averaged over 10g tissue. (a) dipole 5cm length, (b) dipole 25cm length, and (c) dipole 45cm length.

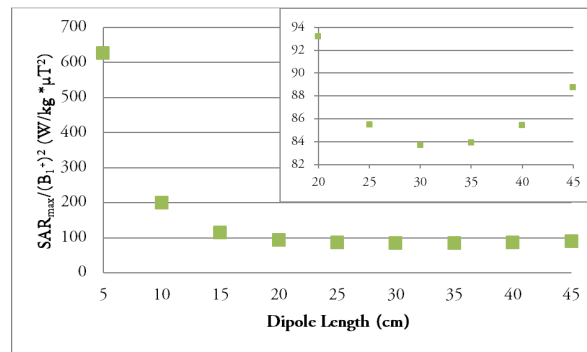
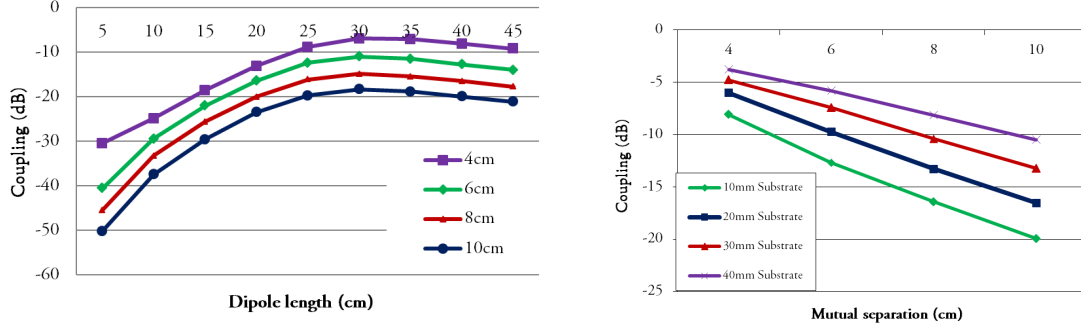


Figure 4-4: Calculated ratio local $SAR_{max} / (B_1^+)^2$ in function of the dipole length.

correspond to a range from 25cm to 40cm, with an optimum value in 30cm length.

Besides the ratio, which links B_1^+ and local SAR_{max} measurements; the other key parameter is coupling. The dipole is thought to be part of a surface array of eight antennas, which may interfere destructively with each other. Simulation results are analyzed from different coordinated planes; through the variation of dipole length, and the variation of mutual distance between identical elements. Figure 4-5a presents coupling values of the dipoles from 5cm to 45cm length in steps of 5cm varying the mutual distance between the antennas while the substrate thickness remains constant (10 mm). For 10 mm substrate thickness, increasing the dipole length is disadvantageous for coupling. Starting from 4cm mutual separation to 10cm, coupling increases with distance. However influence in coupling by mutual distance is more noticeable in short dipoles compared to long ones. It can be inferred that coupling in dipoles

from 30cm to 45cm length remains almost constant just varying with the mutual distance.



(a) Coupling versus dipole length with different separation distances (b) Coupling versus mutual distance with different substrate thicknesses

Figure 4-5: Simulated coupling measurements in the dipole antenna.

From the mutual separation distance, figure 4-5b shows different substrate thicknesses with different separation distances for a dipole length of 40cm. The substrate thickness is proportional to the coupling; with 10mm substrate thickness presenting the best values in coupling from 4cm mutual separation until 10cm separation. In contrast 40mm substrate thickness is producing the highest coupling for all mutual separation distances simulated.

4-1-2 Fractionated Dipole Parameters Simulation Results

Variation in substrate thickness

The fractionated dipole antenna was simulated in the beginning with a substrate thickness of 8mm, and using perspex (PMMA) as substrate material. This substrate thickness study also uses perspex, and starts with a thickness of 10mm until 50mm in steps of 5mm. Figure 4-6 presents two simulated B_1^+ distributions; 10 and 50mm respectively, from both coronal and transversal view.

Surprisingly, the decrease in B_1^+ value at 10cm depth from 10mm to 50mm is just 10% (figure 4-8a). This means substrate thickness has just a slight impact on the magnetic field. In contrast, the SAR distributions (figure 4-7) present a considerable decrement comparing 10mm with 50mm substrate. Average SAR_{max} as a function of the substrate thickness decreases in almost 50% (figure 4-8b), confirming the pattern given by the SAR distributions. Overall, substrate thickness seems to have a stronger influence in the local SAR than compared to the B_1^+ ; as the latter remains stable.

The calculated ratio $SAR_{max}/(B_1^+)^2$ ranges from 10mm to 50mm (figure 4-8c), present a downward trend overall, pointing to the lowest value in 50mm substrate thickness. Note that both B_1^+ and SAR simulations were performed with a single element, in this case a fractionated dipole with meanders.

Until now, it can be partially concluded that substrate thickness has a positive impact in the performance of the fractionated dipole; as with its increment the magnetic field at 10cm depth remains almost constant, SAR decreases, and the ratio kept decreasing. However, the

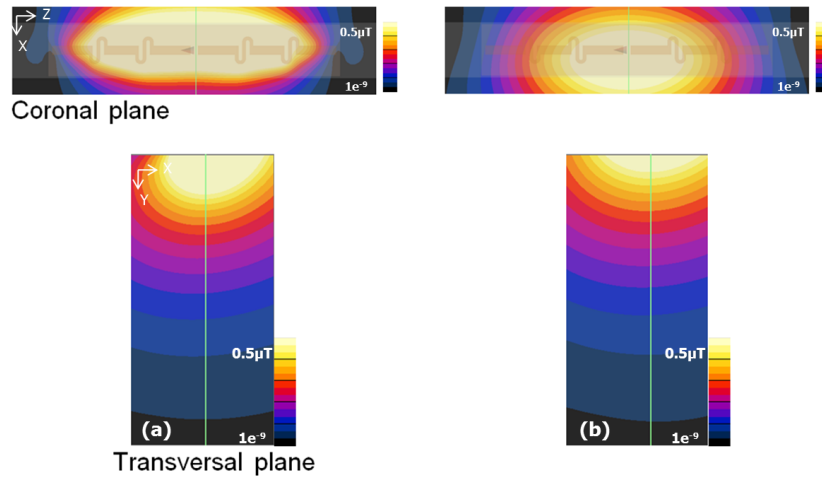


Figure 4-6: Simulated B_1^+ distributions in the coronal x-plane and transversal z-plane directly below the element, linear color scale, normalized for 1W delivered power in function of substrate thickness. (a) FDWM with substrate thickness 10mm, and (b) FDWM with substrate thickness 50mm

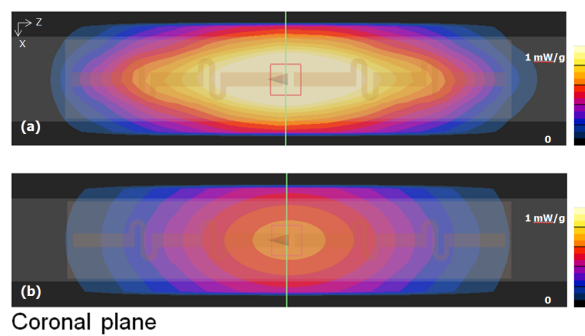


Figure 4-7: Simulated local SAR distributions in the coronal x-plane in function of substrate thickness, linear color scale, normalized for 1W of delivered power and averaged to 10g tissue (a) FDWM with substrate thickness 10mm, and (b) FDWM with substrate thickness 50mm

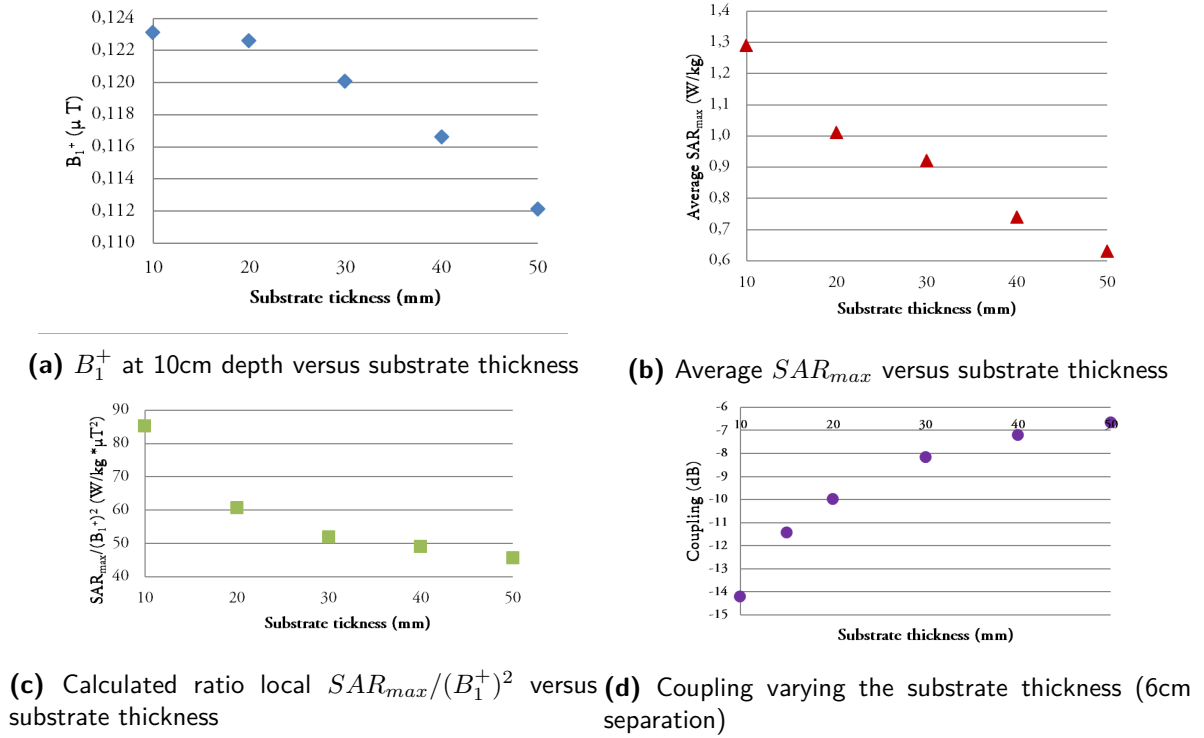


Figure 4-8: Simulated measurements for the fractionated dipole antenna

antenna is thought to be part of a surface array, thus coupling is the next criteria to evaluate to reach a final conclusion about substrate thickness.

Figure 4-8d shows that the substrate thickness is proportional to the coupling. In contrast with partial conclusions obtained from the analysis of both magnetic field, SAR distributions, and the ratio; the coupling is found to be a limiting factor in the performance of the fractionated dipole with meanders. For prostate imaging, optimum substrate thickness ranges between 10 to 20mm.

Variation in number of meanders

The simulated B_1^+ values at 10cm depth with a variation of the number of meanders from zero to ten in steps of two meanders and 16 meanders is shown in figure 4-9a. In general, higher the number of meanders, lower the B_1^+ value. As the number of meanders increases, the B_1^+ distribution at depth starts deforming from a cardioid shape into two lobes located symmetrically. Due to this deformation the maximum B_1^+ value is not located in the centre of the antenna but is displaced to the sides. B_1^+ values from figure 4-9b were taken at directly in the center of the fractionated dipole, and as the number of meanders increases do not coincide with the maximum values.

The variation of meanders was simulated with three different substrate thicknesses: 15mm, 20mm and 30mm (figure 4-9b). The fractionated dipole with four meanders shows the highest B_1^+ values at 10cm depth for the three different substrate thicknesses. Note that the B_1^+ values at 10cm decreases as the substrate and the number of meanders increases.

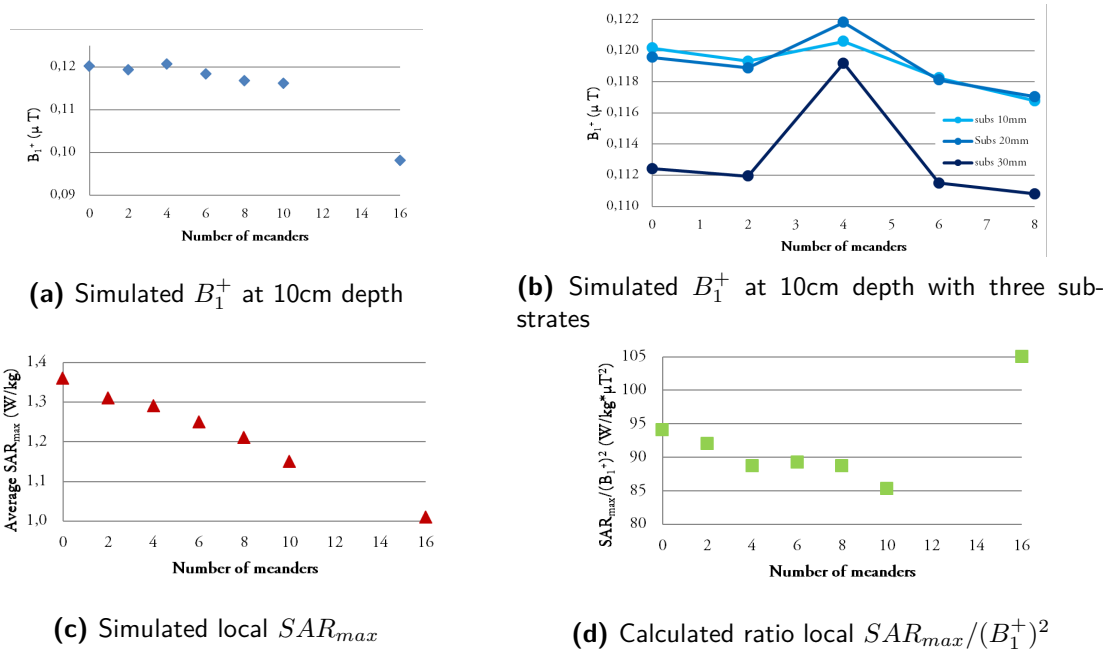


Figure 4-9: Simulated measurements varying the number of meanders

The local SAR_{max} decreases while the number of meanders increases (figure 4-9c). This decrease is gradual; thus the influence from the number of meanders becomes clearer with the ratio. Figure 4-9d presents the ratio local $SAR_{max}/(B_{1at10cm}^+)^2$, with two low values located in four meanders and in ten meanders. It can be said that in spite of a low value of local SAR_{max} in 16 meander, the ratio indicates poor performance, which is due to a low B_1^+ value at 10cm depth.

The coupling in function of the number of meanders illustrates that increasing the number of meanders decreases the coupling between identical elements (table D-7). Despite the lack of improvement shown by the other three analyzed criteria, it is interesting to point this out, as with the variation of substrate thickness, opposite results were found. In general, the number of meanders favors coupling and SAR substantially, but the decrease in the B_1^+ value at 10cm depth is significant (30%).

Variation in form of meanders

The shape of the meanders was varied to observe if it has any influence on the performance of the fractionated dipole. Several shapes and combinations were simulated; figure 4-10 shows the coronal view of the B_1^+ distribution, compared to one of the forms simulated with the fractionated dipole with meanders. The distributions differ one from the other. Taking the B_1^+ distribution as the ideal (figure 4-10(a)), the shape depicted (figure 4-10(b)) is far away from the ideal; which shows three lobes and an irregular distribution along both planes.

The graph (4-11a) shows the B_1^+ value at 10cm depth for some of the simulated shapes. Quantitatively, it is clear that the fractionated dipole with meanders has a deeper penetration in comparison with the other six forms present shown in the graph.

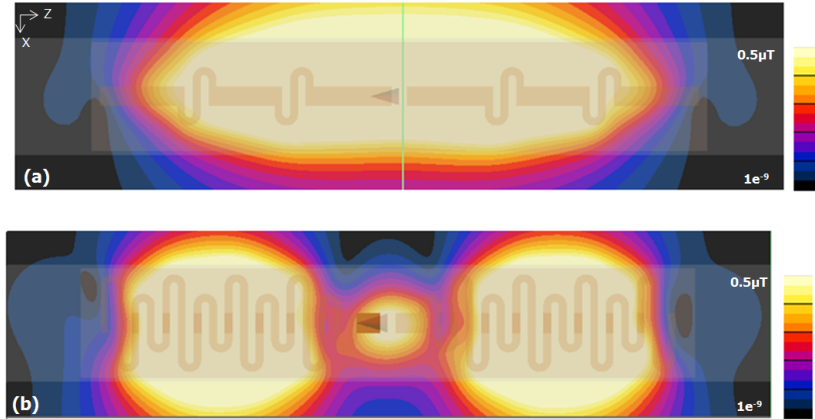
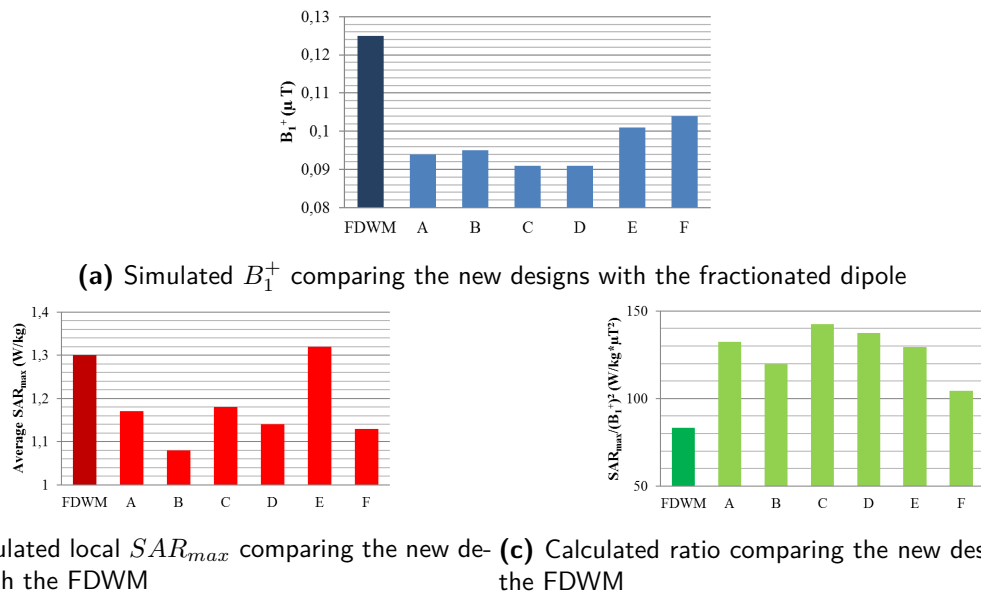


Figure 4-10: Simulated B_1^+ distributions in the coronal x-plane, linear color scale, normalized for 1W of delivered power. (a) fractionated dipole with meanders, and (b) form A



(b) Simulated local SAR_{max} comparing the new designs with the FDWM **(c)** Calculated ratio comparing the new designs with the FDWM

Figure 4-11: Simulated measurements varying the form of meanders

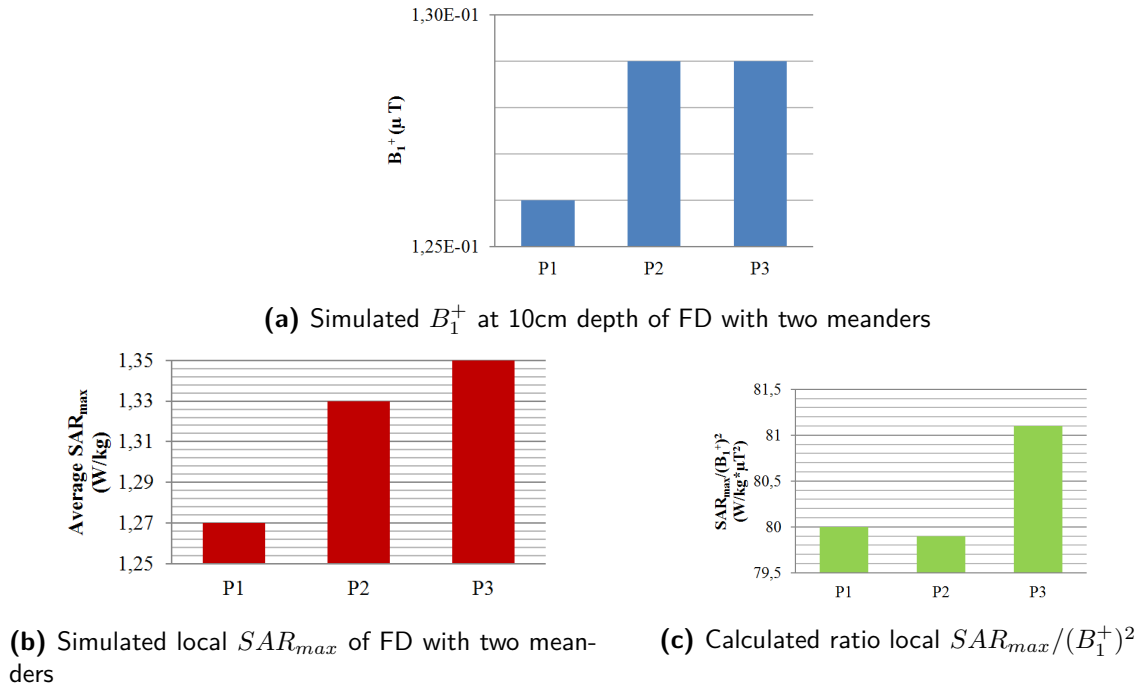


Figure 4-12: Simulated measurements varying the position of meanders where (P1) extremes of the conductor (P2) middle (P3) near the source

In general, the local SAR_{max} value in the different shapes is lower compared to those in the fractionated dipole with meanders (figure 4-11b), with the exception of the form E which is slightly higher than the FDWM value. The ratio $SAR_{max}/(B_{1at10cm}^+)^2$ is higher for all the forms compared with the fractionated dipole, meaning that its efficiency is lower than the FDWM (figure 4-11c). Coupling was not studied because the ratio presented a very poor performance.

Variation in position of meanders

The fractionated dipole has four meanders, distributed along the two conductors. The position was studied with a fractionated dipole with two meanders in order to observe the influence of the position. Both meanders were located in the extremes (P1), in the middle (P2), and finally both near the source (P3). Figure 4-12a shows the B_1^+ values at 10cm depth in three different positions. It can be seen that the B_1^+ values change less than 5% along the conductor (15cm length). The change in the SAR_{max} is slightly higher than 5% compared to the three positions (figure 4-12b). Additionally, the ratio shows less than 5% change, which implies the parameter position of the meander for a fractionated dipole with two meanders and a conductor length of 15cm has a weak influence in the efficiency of the antenna (figure 4-12c).

Variation in conductor length

The conductor length was already studied in an ideal case where the conductor is separated from the phantom by an air gap. This study intends to observe whether in a dipole with

a different substrate material; in this case perspex, current substrate material used in the fractionated dipole with meanders, the efficiency is significantly affected as was observed in the ideal dipole. The B_1^+ distributions from the transversal and coronal view are similar to those distributions in the ideal dipole study. The coronal view images have a green line which points out the maximum value, note that in 45cm length this line is not in the centre but slightly to the right.(Figure 4-13)

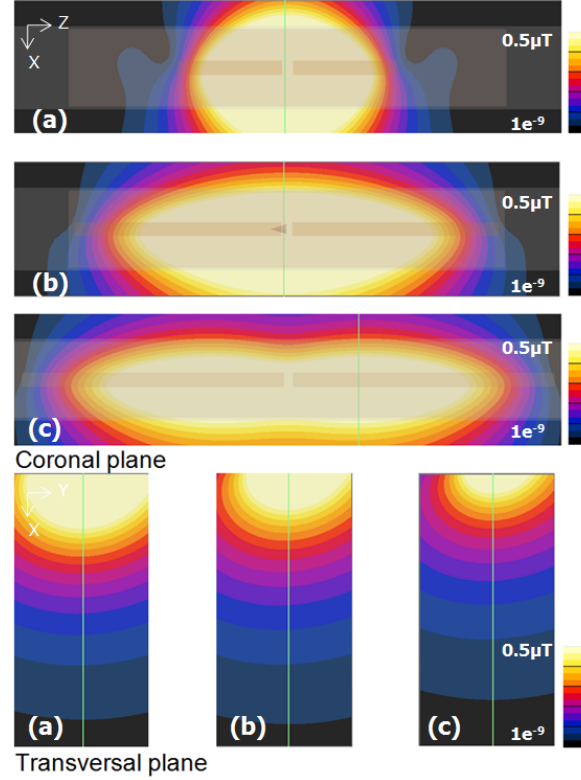


Figure 4-13: Simulated B_1^+ distributions of a dipole in the coronal x-plane and transversal plane y-plane varying the length of the conductor using perspex as substrate material, linear color scale, normalized for 1W of delivered power. (a) dipole 15cm length (b) dipole 30cm length and (b) dipole 45cm length

In general, both B_1^+ values at 10cm depth and local SAR_{max} exhibit a downward trend (figures 4-14a 4-14b), as in the ideal dipole study. The ratio also presents 30cm length as the lowest value for a plain dipole with perspex substrate (figure 4-14c).

Coupling is the last criteria to be analyzed [12, 10]; but instead of analyzing the plain dipole with a perspex substrate, it was considered more interesting to analyze the fractionated dipole with different substrate thicknesses with perspex as a substrate material. Figure 4-14d shows that the coupling decreases as the substrate thickness increases, which is similar to the behavior observed in figure 4-8d with a plain dipole using an air gap instead of perspex substrate.

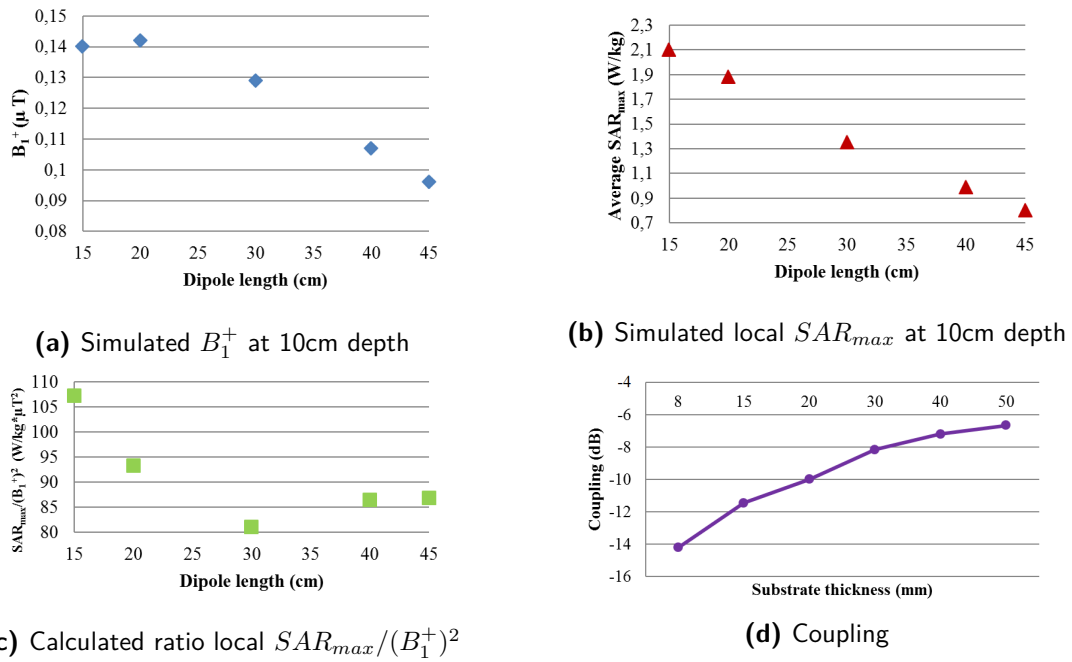


Figure 4-14: Simulated measurements varying the length of the conductor with perspex as substrate material

4-1-3 Special Case: Sinusoidal Antennas Simulation Results

The sinusoidal shape antenna was simulated as a part of the variation in shape of the meanders but as it was studied extensively, it was considered separately from the parameters study. More than 20 different models were simulated in this part first using 8mm substrate (Appendix B); and the best ones were simulated with 20mm substrate thickness.

First of all, the B_1^+ values at 10cm depth in case of the simulated sinusoidal shapes are higher in half of the results compared with the fractionated dipole with meanders (FDWM), however this increase is just about 10% of B_1^+ value. The sinusoidal shapes present B_1^+ distributions similar to the ones observed during the simulations with variation in number of meanders; these distributions have their maximum value at depth not in the centre instead slightly to the sides and the distribution shape symmetrical but split into two lobes at each side of the centre. A comparison of B_1^+ values at 0 and at maximum, and observing the shapes given by the simulation were also taken into account to decide whether the antenna may be a candidate to be an optimized version of the fractionated dipole with meanders. (Figure 4-15)

Sinusoidal shapes have more influence in SAR than in B_1^+ values at 10cm depth. Figures 4-16a, 4-16b, more than 50% decrease in some of the shapes simulated.

In general, most of the sinusoidal shapes present a lower ratio value when compared to the fractionated dipole.

From the ratio and the shape of the distribution, three of the sinusoidal shapes were chosen to simulate coupling. Two of the sinusoidal shapes presented lower coupling values than the fractionated dipole, and one of them show similar behavior referring to coupling but better ratio (figure 4-16c). These two sinusoidal shapes are chosen to be constructed to validate

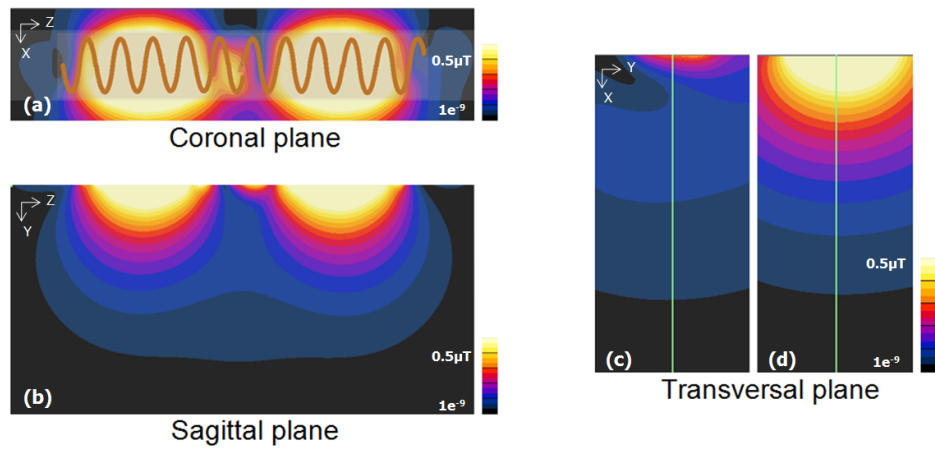
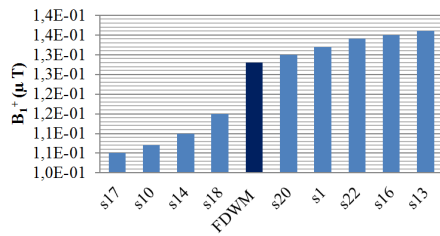
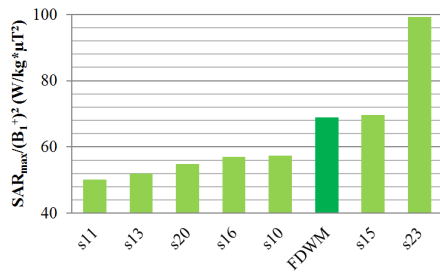


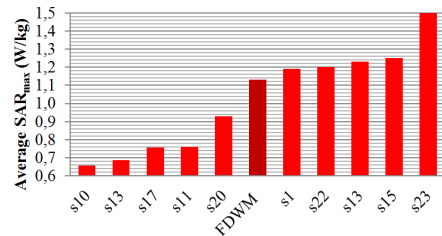
Figure 4-15: Simulated B_1^+ distributions of a dipole in the coronal x-plane and transversal plane y-plane varying the length of the conductor using perspex as substrate material, linear color scale, normalized for 1W of delivered power. (a) dipole 15cm length (b) dipole 30cm length and (b) dipole 45cm length



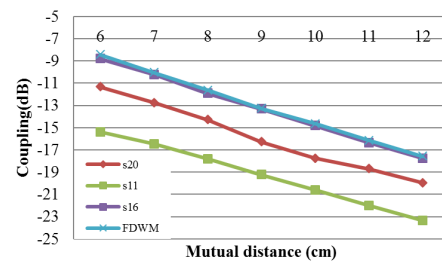
(a) Simulated B_1^+ at 10cm depth



(c) Calculated ratio local $SAR_{max}/(B_1^+)^2$



(b) Simulated local SAR_{max} at 10cm depth



(d) Coupling

Figure 4-16: Simulated measurements of different sinusoidal shapes compared with the fractionated dipole (dark colors)

both B_1^+ values at 10cm depth and coupling. (figure 4-16d)

4-2 RF Antenna Validation

4-2-1 Dipole Validation

Due to the extensive study with the plain dipole, it was chosen to be constructed to observe its performance. The dipole is 30cm length with a substrate thickness of 20mm PMMA and it was matched at 298.2MHz. The B_1^+ maps were performed with one element on the aquarium phantom. Coupling was also measured even though the dipole was not meant to be part of an array but just to validate simulation data.

Coupling was also measured varying the mutual distance between two identical dipoles and was compared with values obtained from the simulation (figure 4-18) .

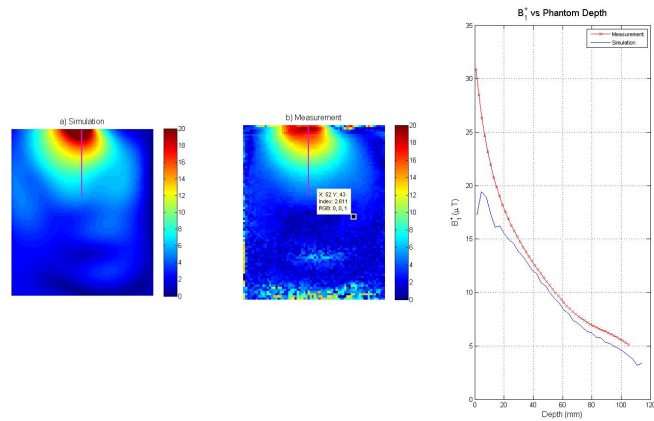
4-2-2 Sinusoidal Antennas Validation

Two of the simulated sinusoidal shapes for construction in order to observe its performance and compare them with the fractionated dipole with meanders. The B_1^+ maps used one of each element on the aquarium phantom, and coupling was measured with two identical elements with a network analyzer varying the mutual distance.

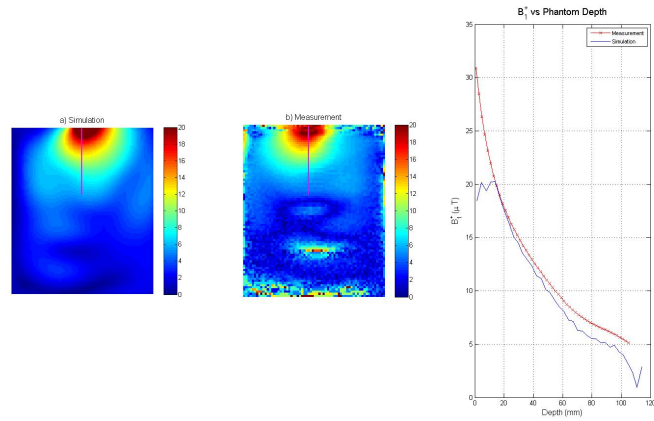
Figure 4-20 show the coupling of both antennas in order to compare simulated and measured values; even though the trend is similar, simulated values are still higher than measured values in this case. This may be due voxelization step during simulations.

4-2-3 In Vivo Measurement

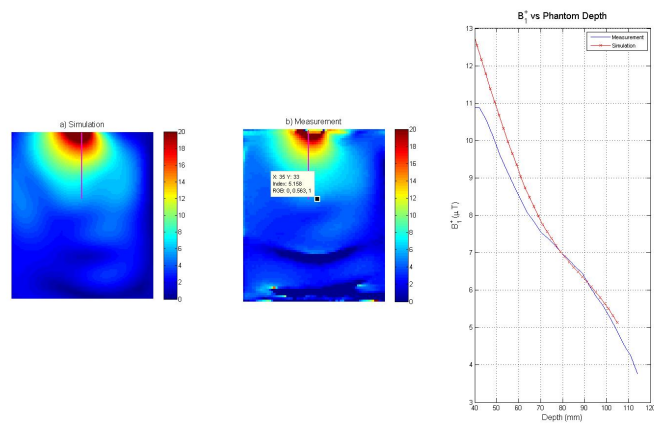
In vivo images were taken with an array of two sinusoidal shape antennas (s20) showing good prostate covering. The elements were matched with the phantom and were tested before using them on the volunteer (Figure 4-21).



(a) Comparison of simulated B_1^+ , measured B_1^+ and profiles with reference magnetic field $13.5\mu\text{T}$ (measurement 6)



(b) Comparison of simulated B_1^+ , measured B_1^+ and profiles with reference magnetic field $13.5\mu\text{T}$ (measurement 3)



(c) Comparison of simulated B_1^+ , measured B_1^+ and profiles with reference magnetic field $7.5\mu\text{T}$ (measurement 5)

Figure 4-17: Validation of B_1^+ measurement of the dipole antenna

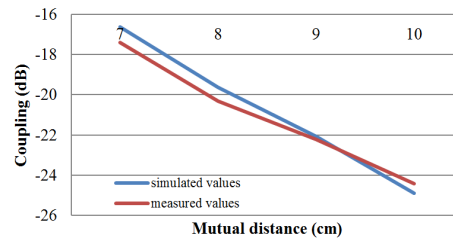
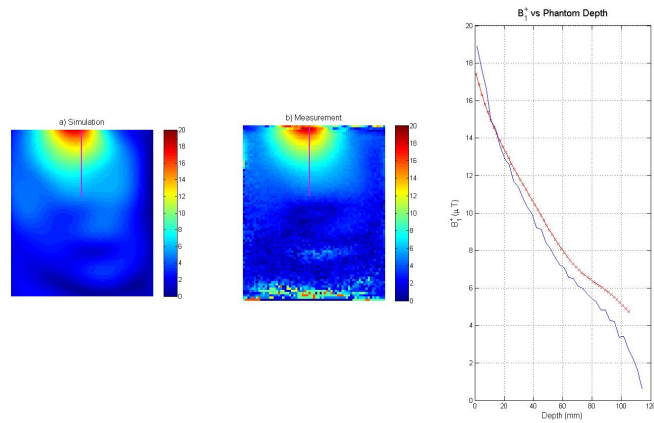
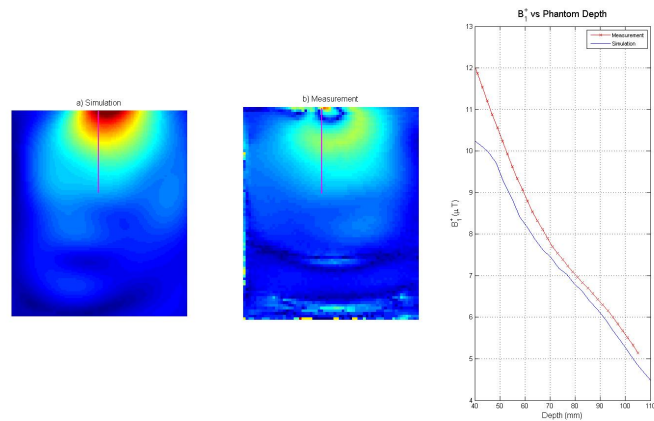


Figure 4-18: Simulated versus measured coupling in a dipole antenna of 30cm length and 10mm substrate thickness



(a) Comparison of simulated B_1^+ , measured B_1^+ and profiles with reference magnetic field $13.5\mu\text{T}$ (measurement 3)



(b) Comparison of simulated B_1^+ , measured B_1^+ and profiles with reference magnetic field $7.5\mu\text{T}$ (measurement 3)

Figure 4-19: Validation of B_1^+ measurement for two snake antennas s11 and s20

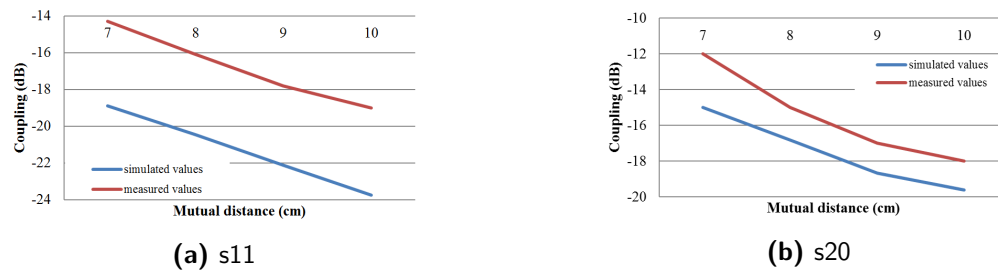


Figure 4-20: Simulated versus measured coupling in two snake antennas s11 and s20

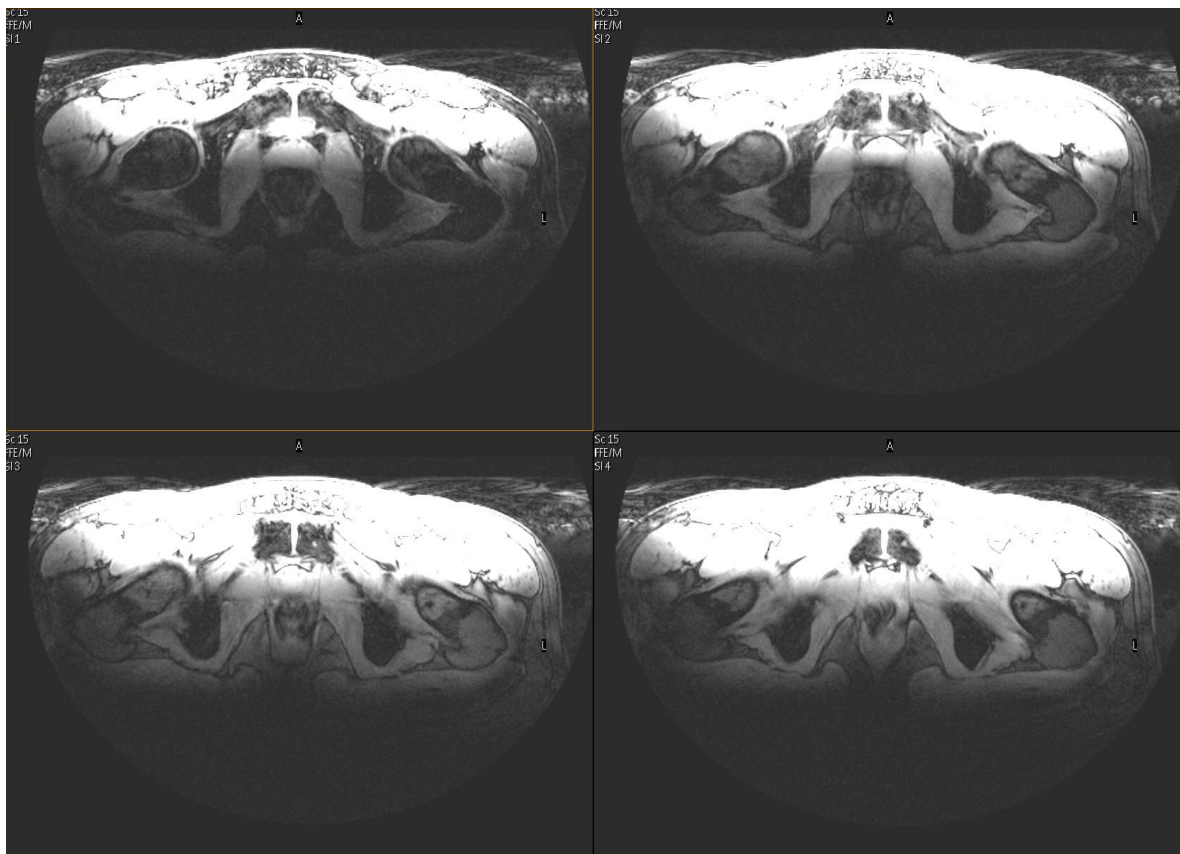


Figure 4-21: Imaging results of array of two sinusoidal shaped antennas on a volunteer. Gradient Echo (GRE) transverse image of prostate and pelvis; TE/TR= 1.44/20 ms; resolution: $1 \times 1 \times 5 \text{ mm}^3$; NSA=2 (Number of Signal averages)

DISCUSSION AND CONCLUSIONS

5-1 Discussion

The optimization of an RF coil for prostate imaging at 7T Magnetic Resonance system is investigated. This RF coil called fractionated dipole with meanders is a coil used for prostate imaging designed following a far-field-based concept recently proposed by *Raaijmakers et al.* [9], who has demonstrated that by using this concept higher transmit B_1 at depth can be obtained; thus increasing the transmit performance necessary to acquire good images from this deeply located organ. This project focused on the improvement of this RF coil in terms of safety and transmit performance. The RF coil consists of a fractionated dipole antenna mounted on an acrylic substrate, and it is used as part of a surface array for MR imaging. Numerical simulations were used to evaluate performance, safety and coupling from new designs in the search of overall improvement. From the simulated results, three designs were constructed for validation purposes. Two different measurements were performed to validate the simulations: B_1 measurements in the 7 Tesla MR scanner and coupling measurements with a network analyzer; these measurements were performed on a phantom with tissue electrical properties. Finally, an in vivo measurement using two identical sinusoidal-shaped snake antennas (s20) aligned on the pelvis was performed to image a healthy prostate.

5-1-1 Dipole Discussion

The first part of this project involved a plain dipole separated from the phantom by an air gap. The dipole was chosen to be studied to characterize its performance and safety in order to compare them with the fractionated dipole and assess its improvements. The main advantage of the dipole is its basic structure which helped to analyze simulation results easily. Two parameters were investigated on this antenna; its length and the air gap distance to the phantom. The findings from simulations indicate that the length of the dipole has a big impact on the B_1^+ radiation profile. Although the radiation pattern has a symmetrical shape through the dipole length variation from 2cm to 45cm, it is no longer homogeneous. The field distribution changes from an spherical shape in the range from 2cm to 30cm dipole length into

a two lobes distribution up to 35cm length dipole, beyond it is no longer useful for prostate imaging, as the B_1^+ maximum value is no longer in the center of the antenna, but distributed. Prostate imaging in 7T Magnetic Resonance requires a homogeneous B_1 distribution with its maximum value located in the centre of the antenna, to ensure a high B_1^+ value in the prostate.

The local SAR also decreases by increasing the length of the dipole, which is ideal; therefore a dipole length that satisfies both criteria can be found. Actually the ratio between the B_1^+ and the average SAR_{max} is calculated to find the optimum performance of the antenna. From the simulations the optimum length given by the ratio, considered as the RF efficiency determiner, is 30cm length; it is important to note that this optimum length differs from the B_1^+ optimum length obtained with 20cm length dipole and also is different from the SAR optimum obtained with a 45cm length dipole.

The coupling was measured varying the length of the dipole and also the mutual distance between two identical elements. The antennas are designed to be part of an array of eight identical elements. The coupling is measured to ensure the elements do not interfere with each other because they are part of a surface array; as expected by increasing the mutual distance between the antennas, decreases the coupling. The optimum length obtained by the ratio was 30cm. In contrast, this dipole length is the one showing the highest coupling values from the range 2cm to 45cm. Improving the coupling with constant length can be done by increasing the mutual distance between the antennas or using a smaller air gap. Figure 4-5a shows decrease in coupling by increasing the mutual distance; but as in practice the eight antennas are part of a belt; this implies a practical limit. Although the increment of air gap shows its benefits for safety; coupling values are significantly affected. Taking into account the results from the three design criteria 30cm length with an air gap of 2 cm is the optimum design from this dipole study.

5-1-2 Fractionated Dipole Parameters Study Discussion

The fractionated dipole with meanders is an antenna used for imaging targets located outside the near field such as the prostate. This antenna is based on a dipole. Our main goal was to optimize this antenna by means of a parameter study, taking some design parameters to find an optimal performance ensuring low values of specific absorption rate (SAR) in the targeted area. The same parameters were studied as in the case of dipole: the fractionated dipole length and the thickness of the substrate using PMMA material as substrate, in order to observe the changes produced by the addition of the meanders and how they benefit the coil performance. In addition, some parameters related to the meanders were investigated such as form, number and shape. In total, five design parameters were evaluated using numerical simulations in terms of radiation depth, power deposition and coupling. This study generated an extensive number of simulations.

The parameters which presented more impact in all the measurements were the conductor length and the substrate thickness. From the conductor length parameter, the ideal length is found from 25 to 35cm, very similar results compared with the ideal dipole from the dipole study. Furthermore, the ideal substrate thickness was found from 15mm to 20mm. In addition, the form and number of meanders show some influence in the performance, especially in the local SAR. In this two parameters variation, the B_1 values obtained were

low, however these variations favored local SAR along with coupling. Thus, in spite of poor efficiency, sinusoidal forms were simulated to explore whether different forms could still bring this benefits in safety and coupling while maintaining high B_1 values at 10cm depth. The position of the meanders along the conductor presented no significant variations in any of the measures, yet it could be possible to observe more variation using a longer conductor.

In general, the coupling, like the local SAR, is a limiting factor for some designs that show good performance efficiency as single elements. The simulations and measurements of the B_1 maps and the coupling of the dipole presented good agreement.

5-1-3 Sinusoidal Antennas Discussion

After the parameters study with the fractionated dipole antenna, lower levels of local SAR were found when varying the number and form of the meanders. Safety is one of the aspects of main concern for 7T MRI, thus these results shown a possible solution to decrease energy power deposition on tissues. For this reason, further designs with sinusoidal shapes were simulated, since it could be considered that an optimum design might be achieved by trying different forms. The shapes were varied in frequency and amplitude. The measures taken from the simulations were the radiation field B_1 , the average local SAR and the coupling.

The aspects analyzed involving the radiation field B_1 during the parameters study, were the pattern, the profile and the value at 10cm depth. In this study it was interesting to see higher values at 10cm compared to the fractionated dipole, while other designs presented lower values. In the case of the average SAR_{max} , the order of variation is higher. Due to these measurements variations, it is not easy to recognize at first view which design is optimum. However, the ratio gives a more straightforward view, helping to filter the designs showing poor performance.

In spite of having found optimum designs based on the ratio, the radiation pattern does not present its maximum value at 10cm depth in the center of the antenna, not in accordance with what is needed for prostate imaging. These radiation patterns presented a two lobes pattern similar to those in the dipoles with 35 to 45 cm length. This study highlights the importance of the radiation distribution in order to assess the usefulness of each particular design. Taking the radiation distribution as a filter, just few designs met the requirements to be compared with the fractionated dipole. From those designs, coupling was measured using two antennas, to observe how the designs impact on the coupling. Note that coupling was found to be a limiting factor during the parameter study, discarding designs that otherwise show efficient performance as single elements.

Two designs, the snake antennas S11 and S20, qualified to be constructed to validate their performance by B_1 mapping and coupling measurements. The simulated B_1 mappings on the phantom are in good agreement with the measurements obtained from the scanner. After comparing these two designs, S20 was chosen to perform an in vivo measurement, which shows the prostate in a healthy subject using an array of two antennas. In contrast, coupling values are higher in the measurements than in the simulations, which might be due to variability in the electrical properties of the phantom, air gaps between phantom and substrate, and antennas matching effects.

Even though it was possible to image prostate with an array of two snake antennas, assessing the safety of this procedure, the improvements gained are smaller in comparison with the

ones gained by the fractionated dipole. Besides, the geometry of sinusoidal shaped antennas is more complex to simulate, construct and match, creating more uncertainty in the results.

5-1-4 Simulation Limitations

Uncertainties in simulations

In the FDTD simulations, a grid had to be defined before running the simulation; the denser the grid the longer the computation time needed to run the simulation. Results are sensitive to the properties and type of grid used, therefore it is important to find a method to define an optimal grid to find reliable results. In this project, for the dipole antenna design different grid sizes were tried until the degree of variability reached a minimum; and this size was used for all the variations applied to the dipole. In both cases, the parameters study of the fractionated dipole antenna and the sinusoidal-shape designs, the structure of the antennas is far more complex compared to the dipole, specially the meanders which have rounded corners. Therefore, it turned out necessary to use bigger grids, smaller minimum steps especially in the antenna structure besides checking every time the voxelization was an identical reproduction of the original design. The voxelization step needs to be checked along with the connections before running the simulation, especially in cases such as the coupling simulation where two elements are simulated. In the case of coupling, it is interesting to observe that from the three antennas, the one showing more agreement between measurements and simulations is the dipole; this might be due to the simplicity of the dipole structure when compared with the other two complex antennas. In order to obtain reliable results with short computing times, the voxelization and the connections were checked. Furthermore, Sencad provides simulation settings as bounding box to ensure the correct representation of the antenna geometry. (Figure 5-1)

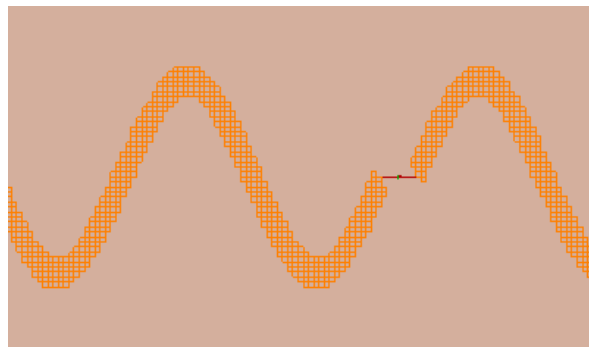


Figure 5-1: Voxelization step in SEMCAD X

Uncertainties in measurement

The setup used for the validation step has some limitations. It is used to measure the B_1^+ in the 7T MR system. Coupling is also measured with two antennas in a network analyzer. The construction of the antennas is a straight forward step as SEMCAD is able to export files to be converted into circuit with the exact geometry design used during the simulations. In the

case of the phantom, the main limitation is generated by its inhomogeneity; consisting of an agarose mix with salt and the possibility of the mix not being homogeneous, will influence the antennas impedance.

The process of matching the antennas to 50 ohms is a task that generates some uncertainties because the network analyzer does not provide stable impedance values. Further, in cases such as the sinusoidal shaped antennas where an inductance was needed, it is not measured but constructed and tuned in the circuit to be as near to 50 ohms as possible. It presents the same behavior when coupling is measured. For the case of 7T MR system, one of the critical steps was to measure the input power to the antennas during B_1^+ measurements, which is needed for correct scaling of the resulting B_1^+ distributions in Matlab. There are still some losses that require further investigation.

Uncertainties in validation

The measurements chosen to validate the data provided by the simulations were the B_1^+ and the coupling; the power deposition was not validated due to the complexity of the measurement and its low reliability. From the parameter study a 30cm length dipole with a 10mm PMMA substrate thickness was constructed to measure its B_1^+ and coupling; both results obtained were in good agreement with the simulations; this is especially noticeable in the coupling comparison.

5-2 Conclusions

This project studied three different antenna designs for prostate imaging at 7T MR: the dipole, the fractionated dipole and the snake antenna. These designs seek to find ways of improving the image quality, and the safety during the imaging process. The dipole was simulated in order to state its performance and safety characteristics, and thus a comparison can be made to measure the improvements gained in the fractionated dipole with the addition of the meanders. The fractionated dipole parameters study was performed to observe which parameters improve the performance of the antenna. Finally, some sinusoidal shapes were simulated as potential optimized designs, especially due to their lower local SAR levels compared with the fractionated dipole. The results achieved with these three studies can be summarized as follows:

The comparison between the dipole and fractionated dipole confirmed that the addition of the meanders improve the SAR levels, keeping the same levels of B_1^+ at 10cm depth, thus guaranteeing good quality prostate images.

The conductor length and the substrate thickness are parameters that can improve the performance of the antenna. For prostate imaging in particular, an optimum length and substrate thickness were found, which not only improve the performance of the imaging process but they also fit clinical purposes.

The sinusoidal shaped antennas presented lower SAR levels, similar B_1^+ levels, and less mutual coupling compared to the fractionated dipole, making them a promising element for prostate imaging. Although improvements were found, they were not significant enough to overcome the uncertainties in the B_1^+ homogeneity generated by these complex geometries.

The results from the studies described above lead us to conclude that the fractionated dipole with meanders is an RF coil optimal for prostate imaging. The parameters study, can be used as reference to design RF coils for different target areas in the body.

5-3 Recommendations

For prostate imaging at 7T MRI, RF coils designed based on far field concept show high RF penetration at depth combined with low power deposition. Additional research using far-field antennas design for different parts located deep in the body is highly recommended. The parameters to be taken into account are the radiation pattern to assure field homogeneity and high penetration depth, average specific absorption rate (SAR), and the ratio $Average SAR_{max}/(B_1^+)^2$ as an efficiency measurement for single elements and in cases such as the prostate where an surface array is used; coupling will be a good measurement to take into account inter-element scattering power losses.

During the dipole study, parameters such as length of the dipole and the substrate thickness were simulated; further investigation can be done for different types of dipole such as the bowtie dipole. Moreover, the width of the dipole, a parameter which was not explored in this project, may be also interesting for future analyzes. Besides the antenna design, another option to optimize its performance is to look for different substrate materials other than perspex (PMMA); which was the material used for all the antennas used throughout this project. Nowadays with current advances in material science, it might be possible to use different materials to optimize the antennas performance.

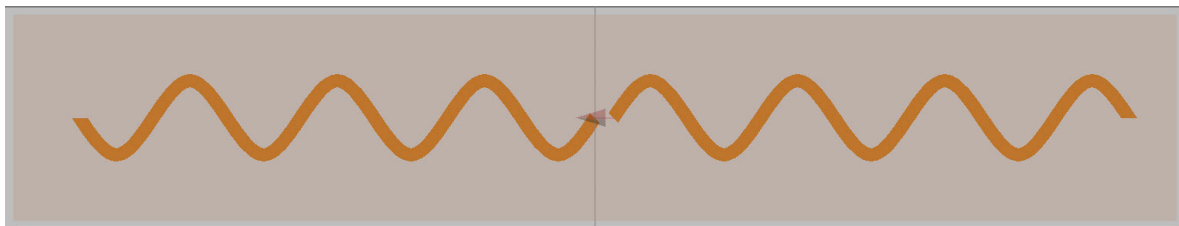
Although this project was focused on optimizing an antenna for prostate imaging, which is a special case for 7T due to the location of the prostate; the results obtained in the parameters study can be used as a base to construct antennas for zones other than prostate.

Additionally, in the parameters study method used for optimization was to vary one parameter at a time while keeping others constant; instead of using this method all the parameters can be varied at the same time for further study. The last method was used once in this project with the Mondrian antenna, a design simulated to observe whether varying all the parameters gives better results than varying one then get the optimum and continue with the others until a concluding optimum is found. As just one design was simulated, more designs can be simulated with this method to find more concluding results than the ones obtained with the Mondrian antenna [Appendix E].

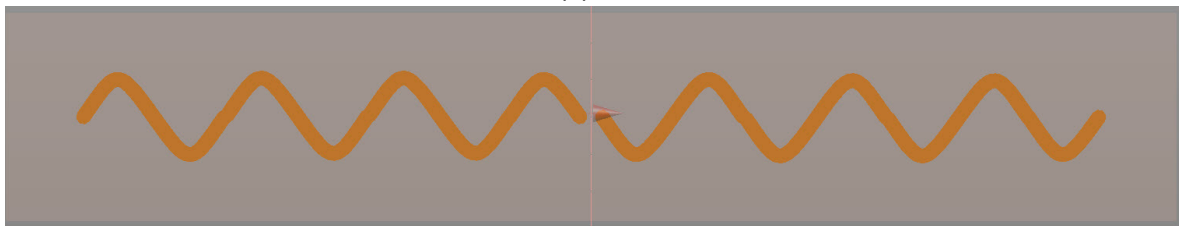
Appendix A

Sinusoidal Shaped Antennas

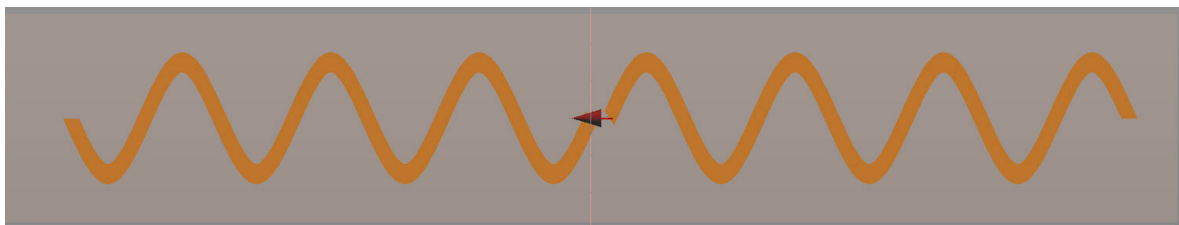
These are some of the 23 sinusoidal antenna designs that were simulated during this thesis project. Two designs: s11 and s20 were chosen for their performance to validate the simulated data.



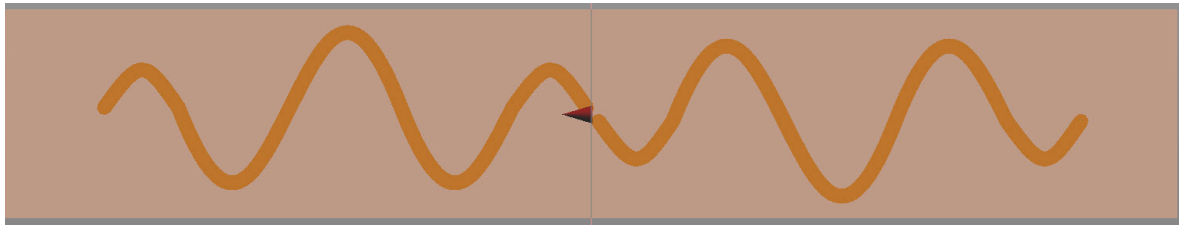
(a) S9



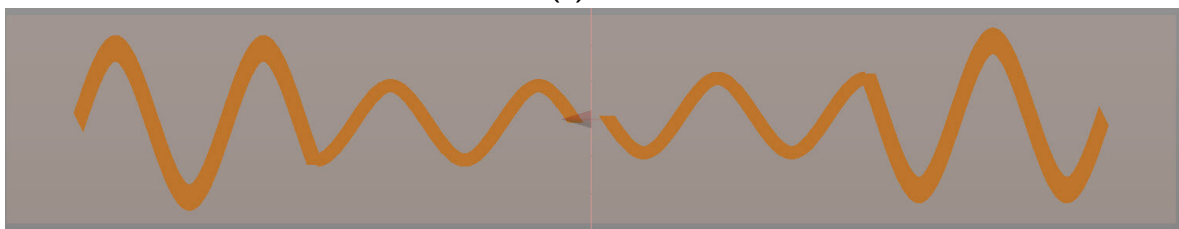
(b) S10



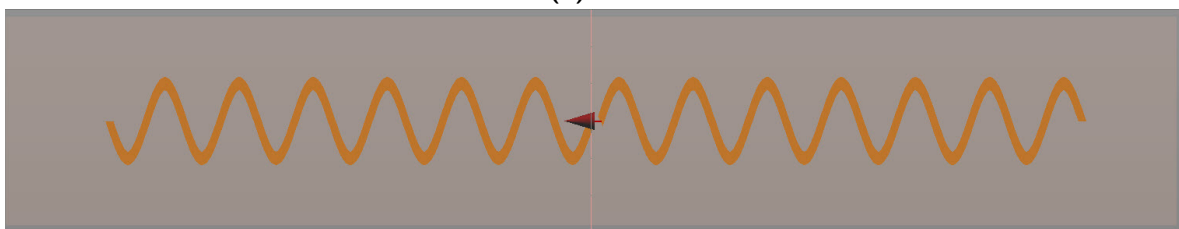
(c) S11



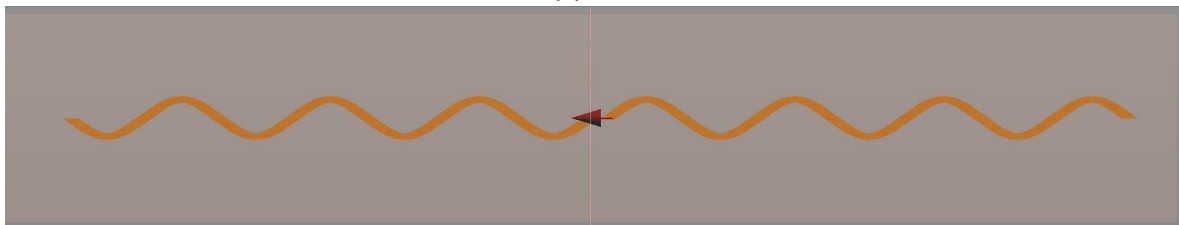
(a) S12



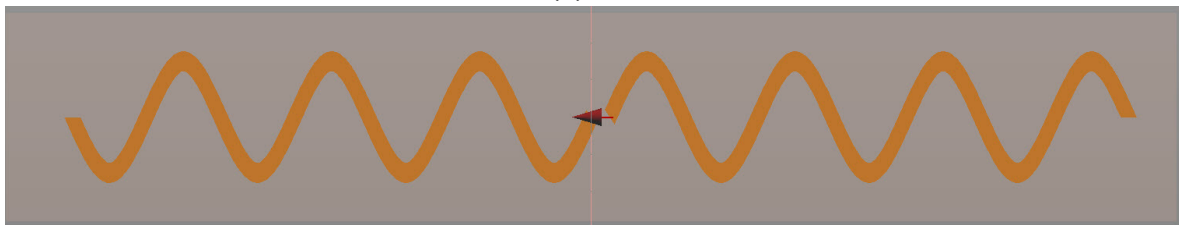
(b) S13



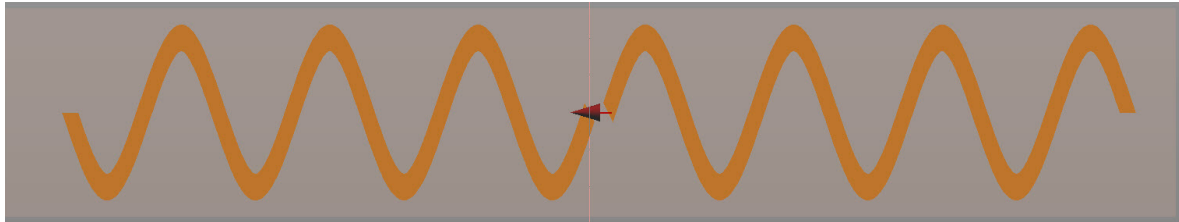
(c) S14



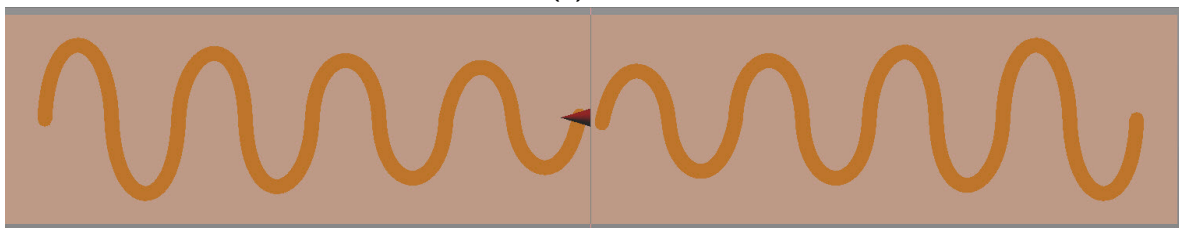
(d) S15



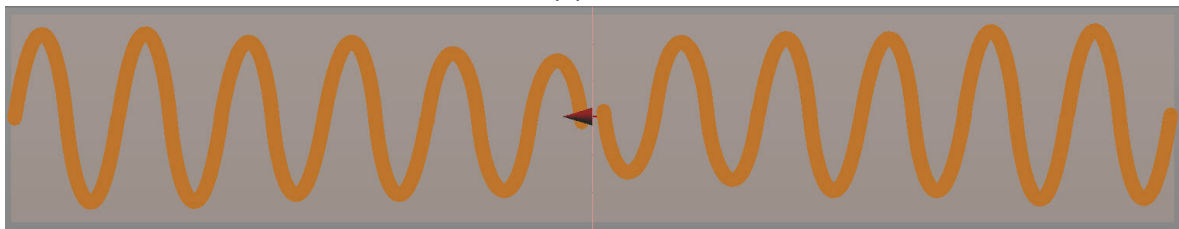
(e) S16



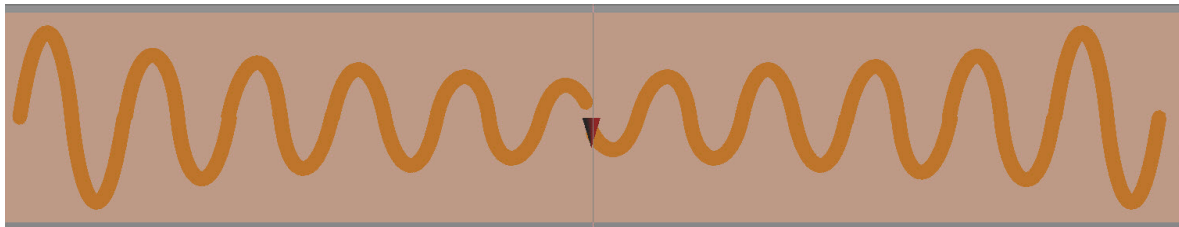
(a) S17



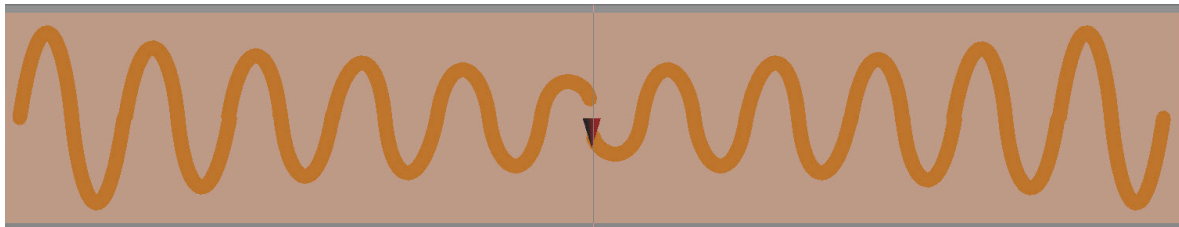
(b) S18



(c) S19



(d) S20



(e) S21

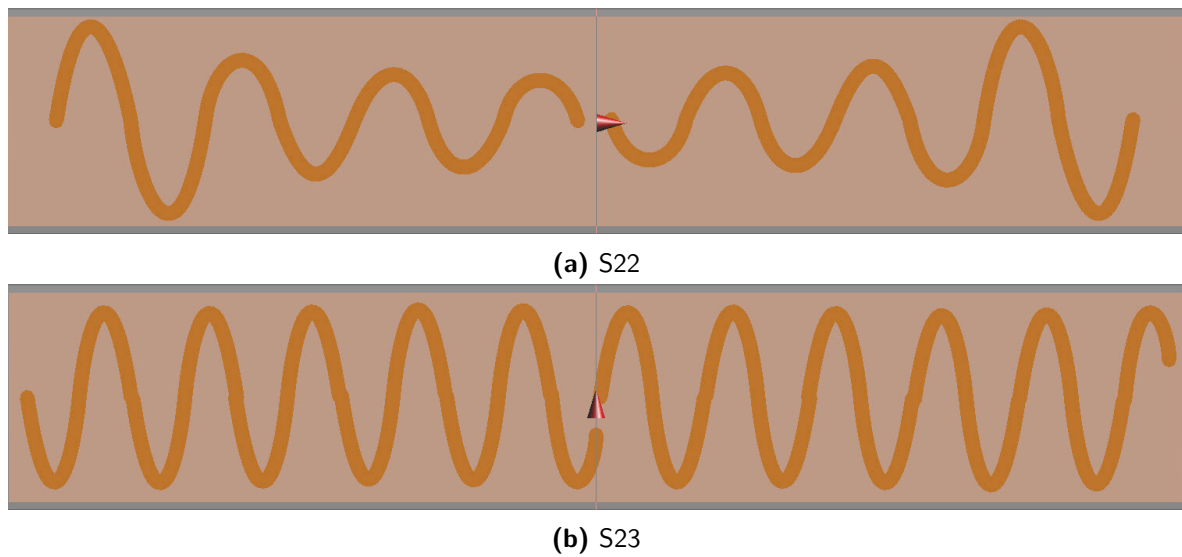


Figure A-4: Simulated sinusoidal antenna designs

Appendix B

Construction of the phantom

After the Semcad X simulations with different RF coil designs were performed, the next step was to validate all the data obtained. The simulated B_1 measurements were validated by measurements performed in a 7T Philips System. The fractionated dipole with meanders antenna made necessary to construct a phantom, due to its size (30cm long), in order to avoid reflections of the magnetic field [32, 33]. The phantom was created by adjusting the electrical conductivity (σ) with NaCl concentration ensuring the same value as in tissue at 300MHz [34], the resonant frequency for 7 Tesla MR system. The values of the properties were 0.4 S/m for electrical conductivity and 80 for relative permittivity.



Figure B-1: Phantom used for B_1^+ measurements in the 7T MR system

The phantom chosen was an acrylic aquarium of 22 x 40 x 25 cm^3 , with a total volume of 22L B-1. The required salinity (g/L) for the requested conductivity (0.4 S/m) was calculated following the equations from Stogryn [35]. These equations calculate the required salinity for a requested conductivity taking into account the room temperature (22°C) and the frequency. Various ratios of water, agarose, salt, and copper sulfate were used in the construction. The quantities for a 22L volume are:



Figure B-2: Small phantom for permittivity measurements

- Agarose: $20\text{g/L} = 440\text{g}$
- Salt: $2\text{g/L} = 44\text{g}$
- Copper sulfate (CuSO_4): $0.9\text{g/L} = 19.8\text{g}$

The copper sulfate was used to shorten the T_1 [36]. The T_1 was measured and found to be around 205ms. Another measurement was permittivity, which gives a value from 80 to 90, provided by A. Van Lier [37].

Appendix C

Actual Flip Angle Imaging Method

The B_1^+ measurements were performed in a Philips 7 Tesla system. The method chosen for imaging was the actual flip-angle (AFI) pulse sequence, which permits fast image-based measurements of the transmitted radiofrequency (RF) field. This method is widely explained in the article “Actual Flip-Angle Imaging in the pulsed steady state: A method for rapid three-dimensional mapping of the transmitted radiofrequency field” [31].

The equation (C-1) used in the Matlab function to process the B_1^+ measurement data is an approximation assuming short TR_1 value of the medium and TR_2 .

$$r \approx \frac{1 + n \cos \alpha}{n + \cos \alpha} \quad (\text{C-1})$$

where $n = TR_2/TR_1$. Note that this equation (C-1) is independent of T_1 measure, giving also an approximated flip angle α :

$$\alpha \approx \frac{rn - 1}{n - r} \quad (\text{C-2})$$

After using this method, the images did not show the B_1^+ measurements (Figure C-1).

In order to obtain good measurements the full equation(C-3) was developed to find the flip angle (equation C-4) taking into account the T_1 .

$$r = \frac{S_2}{S_1} = \frac{1 - E_1 + (1 - E_2)E_1 \cos \alpha}{1 - E_2 + (1 - E_1)E_2 \cos \alpha} \quad (\text{C-3})$$

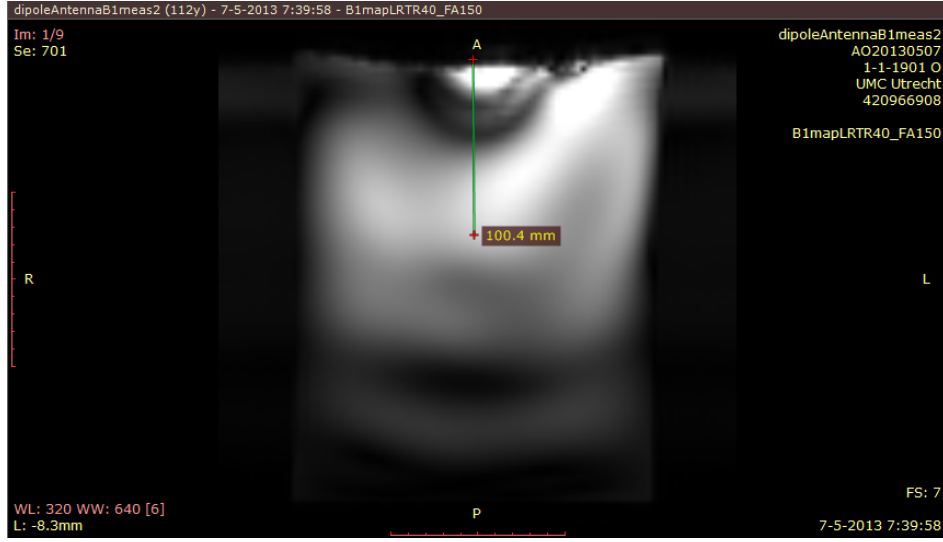


Figure C-1: MR Image showing a black ring

$$\begin{aligned}
 r(1 - E_2 + (1 - E_1)E_2 \cos \alpha) &= 1 - E_1 + (1 - E_2)E_1 \cos \alpha \\
 r - rE_2 + rE_2 \cos \alpha - rE_1E_2 \cos \alpha &= 1 - E_1 + E_1 \cos \alpha - E_1E_2 \cos \alpha \\
 r - rE_2 - 1 + E_1 &= E_1 \cos \alpha - E_1E_2 \cos \alpha - rE_2 \cos \alpha + rE_1E_2 \cos \alpha \\
 r - rE_2 - 1 + E_1 &= \cos \alpha (E_1 - E_1E_2 - rE_2 + rE_1E_2) \\
 \cos \alpha &= \frac{r - rE_2 - 1 + E_1}{E_1 - E_1E_2 - rE_2 + rE_1E_2} \\
 \alpha &= \arccos \frac{r - rE_2 - 1 + E_1}{E_1 - E_1E_2 - rE_2 + rE_1E_2} \quad (C-4)
 \end{aligned}$$

Appendix D

Data from SEMCAD X Simulations

This appendix contains the data extracted from the simulations.

Fractionated Dipole Parameters Study

The fractionated dipole parameters study varied: the length of the dipole, the substrate thickness of the antenna, the number of meanders from 0 to 16, the form of meanders, and the location of the meanders.

Variation in dipole length

The tables D-1, and D-2 show the simulated results when the length of the dipole varies.

Table D-1: Simulated B_1^+ normalized to 1 Watt delivered power, simulated average SAR_{max} and calculated ratio average $SAR_{max}/(B_1^+)^2$ in function of the dipole length

Dipole length (cm)	B_1^+ at 10cm depth (μ T)	Average SAR_{max} (W/kg)	Average $SAR_{max}/(B_1^+)^2$ (W/(kg* μ T ²))
5	0,107	7,18	627,1
10	0,133	3,52	198,9
15	0,144	2,35	114,9
20	0,145	1,96	93,2
25	0,141	1,70	85,5
30	0,133	1,48	83,6
35	0,124	1,29	83,8
40	0,114	1,11	85,4
45	0,104	0,96	88,7

Table D-2: Simulated coupling at different mutual distances in function of the dipole length

Dipole length (cm)	Coupling at 4cm (dB)	Coupling at 6cm (dB)	Coupling at 8cm (dB)	Coupling at 10cm (dB)
5	-30,41724	-40,53256	-45,47836	-50,10734
10	-24,8263	-29,3557	-33,2183	-37,4088
15	-18,5721	-21,9813	-25,5972	-29,5653
20	-13,0674	-16,3875	-19,9534	-23,7623
25	-8,90034	-12,412	-16,0941	-19,7346
30	-6,89129	-10,9421	-14,8091	-18,2887
35	-7,01577	-11,4997	-15,411	-18,815
40	-8,05796	-12,7014	-16,5728	-19,9465
45	-9,27704	-13,9245	-17,7346	-21,0846

Variation in substrate thickness

The tables D-3, D-4, and D-5 show the simulated results when the substrate thickness of the antenna varies.

Table D-3: Simulated B_1^+ normalized to 1 Watt delivered power, simulated average SAR_{max} values normalized to 1W delivered power and calculated ratio average $SAR_{max}/(B_1^+)^2$ in function of the substrate thickness

Substrate thickness (mm)	B_1^+ at 10cm depth (μ T)	Average SAR_{max} (W/kg)	Average $SAR_{max}/(B_1^+)^2$ (W/(kg* μ T ²))
10	0,1231	1,29	85,3
15	0,1216	1,16	69,7
20	0,1226	1,01	60,7
30	0,1201	0,92	52,0
40	0,1166	0,74	49,0
50	0,1121	0,63	45,7

Table D-4: Simulated coupling at different mutual distances in function of the substrate thickness

Substrate thickness (mm)	Coupling at 4cm (dB)	Coupling at 6cm (dB)	Coupling at 8cm (dB)	Coupling at 10cm (dB)
10	-8,1152	-12,7034	-16,4306	-19,9360
20	-6,0408	-9,7569	-13,3063	-16,5296
30	-4,8184	-7,4314	-10,4093	-13,2431
40	-3,7838	-5,8058	-8,1493	-10,5105

Table D-5: Simulated coupling in function of the substrate thickness

Substrate thickness (mm)	Coupling (dB)
10	-14,2019
15	-11,441
20	-9,9903
30	-8,1589
40	-7,2002
50	-6,6695

Variation in number of meanders

The tables D-6, and D-7 show the simulated results when the number of the meanders varies from zero to 16.

Table D-6: Simulated B_1^+ normalized to 1 Watt delivered power, simulated average SAR_{max} values normalized to 1W delivered power and calculated ratio average $SAR_{max}/(B_1^+)^2$ in function of the number of meanders

Number of meanders	B_1^+ at 10cm depth (μT)	Average SAR_{max} (W/kg)	Average $SAR_{max}/(B_1^+)^2$ (W/(kg* μT^2))
0	0,1202	1,36	94,1
2	0,1193	1,31	92,0
4	0,1206	1,29	88,7
6	0,1183	1,25	89,3
8	0,1168	1,21	88,7
10	0,1161	1,15	85,3
16	0,0981	1,01	104,9

Table D-7: Simulated coupling in function of the number of meanders

Number of (meanders)	Coupling (dB)
0	-11,2727
2	-10,9604
4	-11,4410
6	-12,4994
8	-13,7341
16	-17,9123

Variation in form of meanders

The tables D-8, and D-9 show the simulated results when the form of the meanders varies. (Figure D-1)

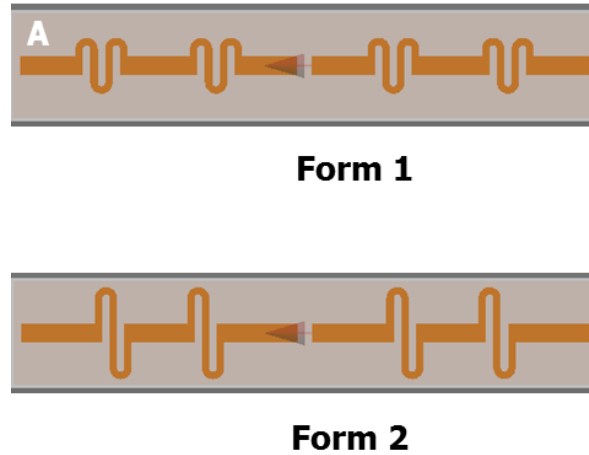


Figure D-1: Variation in the form of the meanders first group of simulations

Table D-8: Simulated B_1^+ normalized to 1 Watt delivered power, simulated average SAR_{max} and calculated ratio average $SAR_{max}/(B_1^+)^2$ in function of the form of meanders (substrate thickness 8mm)

Variation in form	B_1^+ at 10cm depth (μT)	Average SAR_{max} (W/kg)	Average $SAR_{max}/(B_1^+)^2$ (W/(kg* μT^2))
Form A	0,128	1,25	76,3
Form B	0,122	1,17	78,6
FDWM	0,128	1,29	78,7

Table D-9: Simulated B_1^+ normalized to 1 Watt delivered power, simulated average SAR_{max} and calculated ratio average $SAR_{max}/(B_1^+)^2$ in function of the form of meanders (substrate thickness 15mm)

Variation in form	B_1^+ at 10cm depth (μT)	Average SAR_{max} (W/kg)	Average $SAR_{max}/(B_1^+)^2$ (W/(kg* μT^2))
FDWM	0,125	1,30	83,20
Form A	0,094	1,17	132,4
Form B	0,095	1,08	119,6
Form C	0,091	1,18	142,5
Form D	0,091	1,14	137,6
Form E	0,101	1,32	129,4
Form F	0,104	1,13	104,4

Variation in meanders position

The table D-10 shows the simulated results when the position of the meanders varies.

Table D-10: Simulated B_1^+ normalized to 1 Watt delivered power, simulated average SAR_{max} and calculated ratio average $SAR_{max}/(B_1^+)^2$ in function of the position of meanders

Variation in position	B_1^+ at 10cm depth (μT)	Average SAR_{max} (W/kg)	Average $SAR_{max}/(B_1^+)^2$ (W/(kg* μT^2))
P1	0,126	1,27	80,0
P2	0,129	1,33	79,9
P3	0,129	1,35	81,1

Sinusoidal Antennas Study

The tables D-11, and D-12 shows the simulated results obtained with the sinusoidal antenna designs investigated.

Table D-11: Simulated B_1^+ normalized to 1 Watt delivered power, simulated average SAR_{max} and calculated ratio average $SAR_{max}/(B_1^+)^2$ in function of the form of meanders (substrate thickness 8mm)

Sinusoidal antennas	Max B_1^+ at 10cm (μT)	B_1^+ at 10cm (μT)	Average SAR_{max} (W/kg)	Average $SAR_{max}/(B_1^+)^2$ (W/(kg* μT^2))
S1	0,130	0,131	1,230	1,67
S2	0,121	0,127	1,110	68,82
S3	0,121	0,122	1,090	73,23
S4	0,122	0,125	1,500	96,00
S5	0,131	0,131	1,270	74,00
S6	0,123	0,135	1,260	69,14
S7	0,116	0,126	1,370	86,29
S8	0,132	0,134	1,300	72,40
S9	0,133	0,133	1,300	73,49
S10	0,096	0,070	0,867	176,94
S11	0,107	0,112	0,873	69,59
S12	0,106	0,116	1,290	95,87
S13	0,108	0,118	1,320	94,80
S14	0,100	0,086	0,810	109,52
S15	0,100	0,096	0,814	88,32
S16	0,101	0,103	0,827	77,95
S17	0,096	0,071	0,830	164,65
S18	0,101	0,111	0,905	73,45
S19	0,109	0,120	0,946	65,69
S20	0,122	0,128	1,110	67,75
S21	0,133	0,133	1,340	75,75
S22	0,121	0,121	1,210	82,64
S23	0,120	0,127	1,110	68,82

Table D-12: Simulated B_1^+ normalized to 1 Watt delivered power, simulated average SAR_{max} and calculated ratio average $SAR_{max}/(B_1^+)^2$ in function of the form of meanders (substrate thickness 20mm)

Sinusoidal antennas	Max B_1^+ at 10cm (μT)	B_1^+ at 10cm (μT)	Average SAR_{max} (W/kg)	Average $SAR_{max}/(B_1^+)^2$ (W/(kg* μT^2))
S1	0,102	0,107	0,657	57,39
S2	0,113	0,123	0,760	50,23
S3	0,121	0,122	0,989	66,45
S4	0,108	0,115	0,687	51,95
S5	0,102	0,110	0,773	63,88
S6	0,101	0,105	0,757	68,66
S7	0,115	0,115	0,778	58,83
S8	0,132	0,132	1,190	68,29
S9	0,121	0,127	0,980	60,76
S10	0,129	0,130	0,928	54,91
S11	0,134	0,134	1,050	58,48
S12	0,132	0,134	1,200	66,83
S13	0,122	0,123	1,500	99,15
S14	0,136	0,136	1,230	66,50
S15	0,127	0,128	1,070	65,31
S16	0,134	0,134	1,250	69,61
S17	0,135	0,135	1,040	57,06
S18	0,102	0,107	0,657	57,39
S19	0,113	0,123	0,760	50,23
S20	0,121	0,122	0,989	66,45
S21	0,108	0,115	0,687	51,95
S22	0,102	0,110	0,773	63,88
S23	0,101	0,105	0,757	68,66

Appendix E

Mondrian Antenna

The Mondrian antenna (figure E-1) was designed varying all the parameters at the same time.

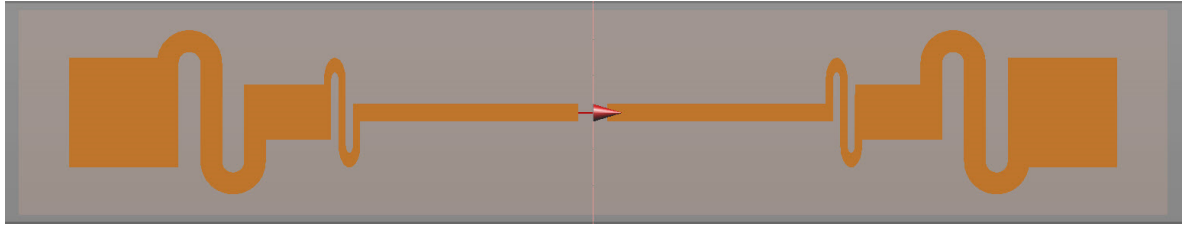


Figure E-1: Mondrian Antenna

The table E-1 shows the simulated results compared to the fractionated dipole with meanders antenna and a sinusoidal antenna. It is interesting to observe that the variation of all parameters produced a design with similar results compared to the other two designs. However, the impact of each parameter is unknown, due to the variation of all of them at the same time. In this project this is considered as a drawback, as one of the goals is to define the parameters having more impact on the different measurements.

Table E-1: Comparison of simulated results between Mondrian antenna, fractionated dipole and sinusoidal antenna

Variation in form	B_1^+ at 10cm depth (μT)	Average SAR_{max} (W/kg)	Average $SAR_{max}/(B_1^+)^2$ (W/(kg* μT^2))
Mondrian Antenna	0,125	1,30	83,2
Fractionated dipole	0,128	1,29	78,7
Sinusoidal Antenna	0,130	1,23	72,8

Bibliography

- [1] T. S. Ibrahim, Y.-K. Hue, and L. Tang, “Understanding and manipulating the RF fields at high field MRI,” *NMR in Biomedicine*, vol. 22, no. 9, pp. 927–936, 2009.
- [2] J. T. Vaughan and J. R. Griffiths, *RF Coils for MRI*. John Wiley & Sons, Dec. 2012.
- [3] V. Mikla, *Medical Imaging Technology*. Elsevier, July 2013.
- [4] J. Hennig and O. Speck, *High-Field MR Imaging*. Springer, 2012.
- [5] J. Vaughan, M. Garwood, C. Collins, W. Liu, L. DelaBarre, G. Adriany, P. Andersen, H. Merkle, R. Goebel, M. Smith, and K. Ugurbil, “7T vs. 4T: RF power, homogeneity, and signal-to-noise comparison in head images,” *Magnetic Resonance in Medicine*, vol. 46, no. 1, pp. 24–30, 2001.
- [6] T. S. Ibrahim, R. Lee, A. M. Abduljalil, B. A. Baertlein, and P.-M. L. Robitaille, “Dielectric resonances and B1 field inhomogeneity in UHFMRI: computational analysis and experimental findings,” *Magnetic Resonance Imaging*, vol. 19, pp. 219–226, Feb. 2001.
- [7] G. J. Metzger, C. Snyder, C. Akgun, T. Vaughan, K. Ugurbil, and P.-F. Van de Moortele, “Local B1+ shimming for prostate imaging with transceiver arrays at 7T based on subject-dependent transmit phase measurements,” *Magnetic Resonance in Medicine*, vol. 59, no. 2, pp. 396–409, 2008.
- [8] J. T. Vaughan, C. J. Snyder, L. J. DelaBarre, P. J. Bolan, J. Tian, L. Bolinger, G. Adriany, P. Andersen, J. Strupp, and K. Ugurbil, “Whole-body imaging at 7T: Preliminary results,” *Magnetic Resonance in Medicine*, vol. 61, no. 1, pp. 244–248, 2009.
- [9] A. J. E. Raaijmakers, O. Ipek, D. W. J. Klomp, C. Possanzini, P. R. Harvey, J. J. W. Lagendijk, and C. a. T. van den Berg, “Design of a radiative surface coil array element at 7T: The single-side adapted dipole antenna,” *Magnetic Resonance in Medicine*, vol. 66, no. 5, pp. 1488–1497, 2011.

- [10] O. Ipek, A. J. E. Raaijmakers, D. W. J. Klomp, J. J. W. Lagendijk, P. R. Luijten, and C. A. T. v. d. Berg, "Characterization of transceive surface element designs for 7 tesla magnetic resonance imaging of the prostate: radiative antenna and microstrip," *Physics in Medicine and Biology*, vol. 57, p. 343, Jan. 2012.
- [11] J. Wang, Q. X. Yang, X. Zhang, C. M. Collins, M. B. Smith, X.-H. Zhu, G. Adriany, K. Ugurbil, and W. Chen, "Polarization of the RF field in a human head at high field: A study with a quadrature surface coil at 7.0T," *Magnetic Resonance in Medicine*, vol. 48, no. 2, pp. 362–369, 2002.
- [12] B. Keong Li, F. Liu, and S. Crozier, "Focused, eight-element transceive phased array coil for parallel magnetic resonance imaging of the chest: Theoretical considerations," *Magnetic Resonance in Medicine*, vol. 53, no. 6, pp. 1251–1257, 2005.
- [13] O. Ipek, A. J. Raaijmakers, J. J. Lagendijk, P. R. Luijten, and C. A. T. van den Berg, "Intersubject local SAR variation for 7T prostate MR imaging with an eight-channel single-side adapted dipole antenna array," *Magnetic Resonance in Medicine*, 2013.
- [14] R. G. Pinkerton, J. P. Near, E. A. Barberi, R. S. Menon, and R. Bartha, "Transceive surface coil array for MRI of the human prostate at 4T," *Magnetic Resonance in Medicine*, vol. 57, pp. 455–458, Feb. 2007.
- [15] C. M. Collins, W. Liu, J. Wang, R. Gruetter, J. T. Vaughan, K. Ugurbil, and M. B. Smith, "Temperature and SAR calculations for a human head within volume and surface coils at 64 and 300 MHz," *Journal of Magnetic Resonance Imaging*, vol. 19, no. 5, pp. 650–656, 2004.
- [16] P. Reimer, P. Parizel, J. Meaney, and F. Stichnoth, *Clinical MR Imaging*. Springer, third ed., 2010.
- [17] O. Rouviere, R. P. Hartman, and D. Lyonnet, "Prostate MR imaging at high-field strength: evolution or revolution?," *European radiology*, vol. 16, pp. 276–284, Feb. 2006.
- [18] P. Davidovits, *Physics in Biology and Medicine*. Elsevier, third ed., 2008.
- [19] J. L. Prince and J. Links, *Medical Imaging Signals and Systems*. Prentice Hall, Apr. 2005.
- [20] M. A. Haidekker, *Medical Imaging Technology*. Springer, 2013.
- [21] P. A. Bottomley and E. R. Andrew, "RF magnetic field penetration, phase shift and power dissipation in biological tissue: implications for NMR imaging," *Physics in Medicine and Biology*, vol. 23, p. 630, July 1978.
- [22] O. P. Gandhi and X. B. Chen, "Specific absorption rates and induced current densities for an anatomy-based model of the human for exposure to time-varying magnetic fields of MRI," *Magnetic Resonance in Medicine*, vol. 41, pp. 816–823, Apr. 1999.
- [23] S. M. Wright and L. L. Wald, "Theory and application of array coils in MR spectroscopy," *NMR in Biomedicine*, vol. 10, no. 8, pp. 394–410, 1997.

-
- [24] E. Moser, F. Stahlberg, M. E. Ladd, and S. Trattnig, “7T MR from research to clinical applications?,” *NMR in Biomedicine*, vol. 25, pp. 695–716, May 2012.
 - [25] P. A. Bandettini, R. Bowtell, P. Jezzard, and R. Turner, “Ultrahigh field systems and applications at 7T and beyond: progress, pitfalls, and potential,” *Magnetic Resonance in Medicine*, vol. 67, pp. 317–321, Feb. 2012.
 - [26] P.-F. Van de Moortele, C. Akgun, G. Adriany, S. Moeller, J. Ritter, C. M. Collins, M. B. Smith, J. T. Vaughan, and K. Ugurbil, “B1 destructive interferences and spatial phase patterns at 7T with a head transceiver array coil,” *Magnetic Resonance in Medicine*, vol. 54, pp. 1503–1518, Dec. 2005.
 - [27] W. D. Callister and D. G. Rethwisch, *Materials Science and Engineering*. Wiley, 9th ed., July 2014.
 - [28] B. van den Bergen, C. A. van den Berg, D. W. Klomp, and J. J. Lagendijk, “SAR and power implications of different RF shimming strategies in the pelvis for 7T MRI,” *Journal of Magnetic Resonance Imaging*, vol. 30, no. 1, pp. 194–202, 2009.
 - [29] P.-M. Robitaille and L. Berliner, *Ultra High Field Magnetic Resonance Imaging*. Springer, 2006.
 - [30] O. Ipek, A. Raaijmakers, J. Lagendijk, P. Luijten, and C. van den Berg, “Optimization of the radiative antenna for 7T magnetic resonance body imaging,” *Concepts in Magnetic Resonance Part B: Magnetic Resonance Engineering*, vol. 43B, no. 1, pp. 1–10, 2013.
 - [31] V. L. Yarnykh, “Actual flip-angle imaging in the pulsed steady state: a method for rapid three-dimensional mapping of the transmitted radiofrequency field,” *Magnetic Resonance in Medicine*, vol. 57, pp. 192–200, Jan. 2007.
 - [32] Q. X. Yang, J. Wang, C. M. Collins, M. B. Smith, X. Zhang, K. Ugurbil, and W. Chen, “Phantom design method for high-field MRI human systems,” *Magnetic Resonance in Medicine*, vol. 52, no. 5, pp. 1016–1020, 2004.
 - [33] B. Beck, K. Jenkins, J. Rocca, and J. Fitzsimmons, “Tissue-equivalent phantoms for high frequencies,” *Concepts in Magnetic Resonance Part B: Magnetic Resonance Engineering*, vol. 20B, pp. 30–33, Feb. 2004.
 - [34] C. Gabriel and S. Gabriel, “Compilation of the dielectric properties of body tissues at RF and microwave frequencies,” Technical AL/OE-TR_1996-0037, Brooks Air Force, 1996.
 - [35] A. Stogryn, “Equations for calculating the dielectric constant of saline water (correspondence),” *IEEE Transactions on Microwave Theory and Techniques*, vol. 19, pp. 733–736, Aug. 1971.
 - [36] M. D. Mitchell, H. L. Kundel, L. Axel, and P. M. Joseph, “Agarose as a tissue equivalent phantom material for NMR imaging,” *Magnetic Resonance Imaging*, vol. 4, no. 3, pp. 263–266, 1986.
 - [37] A. L. van Lier, D. O. Brunner, K. P. Pruessmann, D. W. Klomp, P. R. Luijten, J. J. Lagendijk, and C. A. van den Berg, “B1+ phase mapping at 7T and its application for in

vivo electrical conductivity mapping,” *Magnetic Resonance in Medicine*, vol. 67, no. 2, pp. 552–561, 2012.